

 Open access • Journal Article • DOI:10.1177/0021998319877221

Energy absorption capacity of composite thin-wall circular tubes under axial crushing with different trigger initiations: — [Source link](#)

J.-E. Chambe, Christophe Bouvet, Olivier Dorival, Jean-François Ferrero

Institutions: University of Toulouse

Published on: 01 May 2020 - Journal of Composite Materials (SAGE PublicationsSage UK: London, England)

Topics: Composite number and Dissipation

Related papers:

- [A unified approach to progressive crushing of fibre-reinforced composite tubes](#)
- [Energy Absorption of Composite Materials.](#)
- [Axial splitting of empty and foam-filled circular composite tubes – An experimental study](#)
- [A Study on the energy absorption characteristics of GFRP circular tubes fabricated by the filament winding method](#)
- [Improved Energy Absorption Mechanism: Expansion of Circular Tubes by Rigid Tubes During the Axial Crushing](#)

Share this paper:    

View more about this paper here: <https://typeset.io/papers/energy-absorption-capacity-of-composite-thin-wall-circular-371j12wabx>



Open Archive Toulouse Archive Ouverte

OATAO is an open access repository that collects the work of Toulouse researchers and makes it freely available over the web where possible

This is an author's version published in: <http://oatao.univ-toulouse.fr/24339>

Official URL:

<https://doi.org/10.1177/0021998319877221>

To cite this version:

Chambe, Jean-Emmanuel and Bouvet, Christophe and Dorival, Olivier and Ferrero, Jean-François Energy absorption capacity of composite thin-wall circular tubes under axial crushing with different trigger initiations. (In Press: 2019) Journal of Composite Materials. 1-24. ISSN 0021-9983

Any correspondence concerning this service should be sent to the repository administrator: tech-oatao@listes-diff.inp-toulouse.fr

Energy absorption capacity of composite thin-wall circular tubes under axial crushing with different trigger initiations

JE Chambe¹, C Bouvet¹ , O Dorival^{1,2} and JF Ferrero¹

Abstract

The purpose of this study is to evaluate and compare the ability of various composite structures to dissipate the energy generated during a crash. To this end, circular composite tubes were tested in compression in order to identify their behavior and determine their absorbing capabilities using the specific energy absorption (energy absorbed per unit weight). Several composite tubular structures with different materials and architectures were tested, including hybrid composition of carbon–aramid and hybrid configuration of 0/90 UD with woven or braided fabric. Several inventive and experimental trigger systems have been tested to try and enhance the absorption capabilities of the tested structures. Specific energy absorption values up to 140 kJ.kg^{-1} were obtained, achieving better than most instances from the literature, reaching around 80 kJ.kg^{-1} . Specimens with 0° -oriented fibers coincidental with the direction of compression reached the highest specific energy absorption values while those with no fiber oriented in this direction performed poorly. Moreover, it has consequently been established that in quasi-static loading, a unidirectional laminate oriented at 0° and stabilized by woven plies strongly meets the expectations in terms of energy dissipation. Incidentally, an inner constrained containment is more effective in most cases, reducing the initial peak load without drastically reducing the specific energy absorption value.

Keywords

Crushing, composite tubes, energy dissipation, specific energy absorption, aeronautics

Introduction


CFRP are known to be effective energy absorbing structures, due to the highly dissipative damage mechanisms involved during severe solicitations.^{1–4} For that reason, in addition to their lightness combined with interesting mechanical properties, they are present in various domains: automotive,^{5–7} railway,^{8,9} aeronautics aircrafts,^{10,11} and helicopters,^{12–14} all of which may be subjected to brutal impact resulting in a violent crash.

Damage mechanisms resulting from the crushing of composite structures have been identified on CFRP plates^{15–17} and tubes^{2,3,10,12,18–20,21} structures. Failure mechanisms that contribute the most to the energy dissipation depend on various factors that include delamination, bending, kinking, and fracture of the fibers as well as fracture of the matrix.⁵

Two main failure mechanisms for composite tubular structures have been identified as either catastrophic or progressive failure (Figure 1).^{2,18} For the latter failure

mode, a distinction can be made as the composite tube may undergo progressive folding or progressive crushing¹⁹ (Figure 1). During the first case, composite tube walls progressively fold under successive local buckling (similar to shell buckling) when loaded in axial compression. The extremity of the tube yields in buckle mode, leading to hinge formation and progressive folding; the folded zone then grows progressively down the tube wall. For the second case, the tube collapses as a result of successive brittle fractures. The extremity of the tube breaks leading to the splaying of the tube's wall and multiple fragmentations. Local fracture occurs at the crush front; splaying and micro-fractures

¹Institut Clément Ader, Université de Toulouse, France

²Icam, site de Toulouse, France 

Corresponding author:

C Bouvet, Institut Clément Ader 3, rue Caroline Aigle, Toulouse 31400, France.

Email: christophe.bouvet@isae.fr

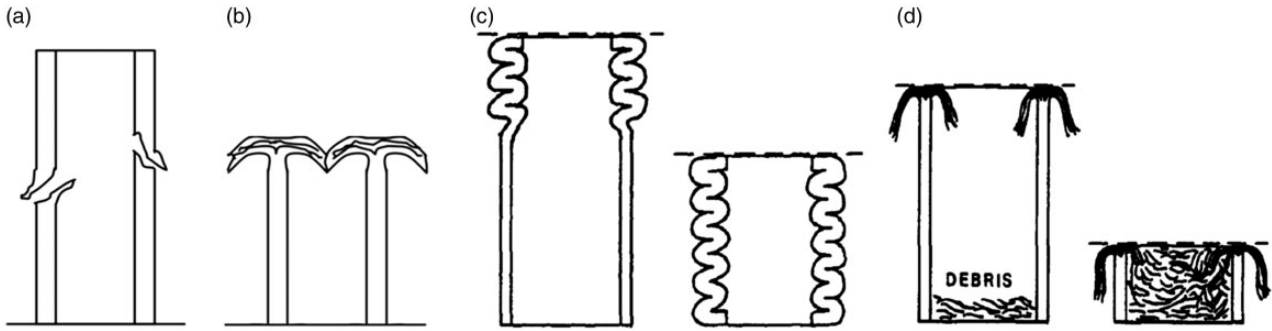


Figure 1. Catastrophic (a) and progressive (b) failure,^{2,18} progressive folding (c), and crushing (d).¹⁹

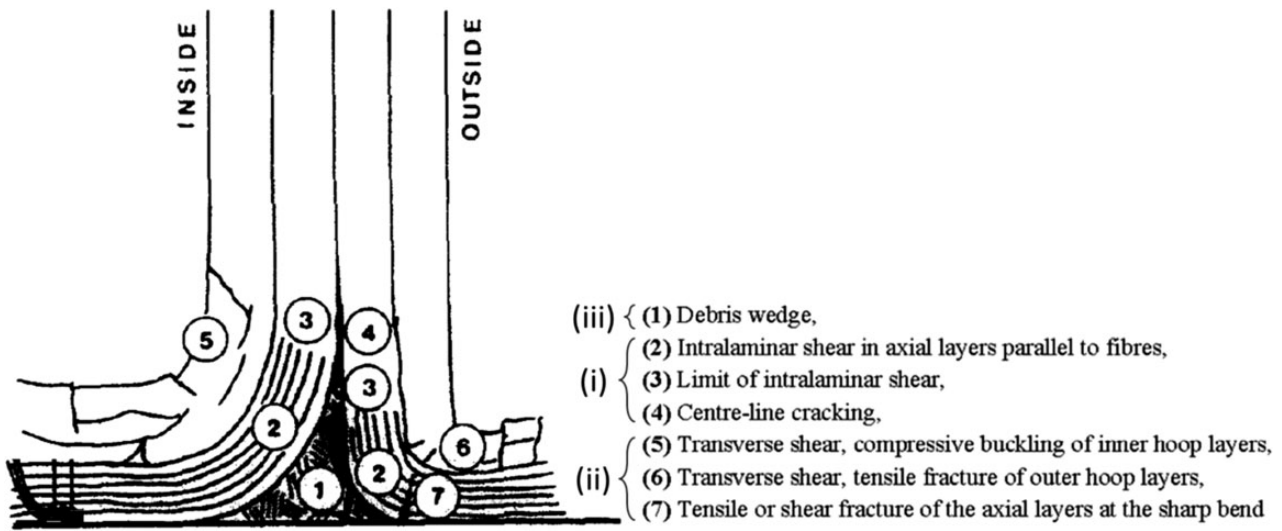


Figure 2. Major damage mechanisms occurring at the crush zone (adapted from Hull¹⁹).

then propagate down the tube.¹⁹ Such a rupture mode tends to generate random sized debris.

In progressive crushing mode, damage mechanisms at the structural scale may be summed up into three types: (i) splaying, (ii) fragmentation, and (iii) debris creation and accumulation^{17,19,21} (Figure 2).

Fragmentation might occur at two levels: under the tip of the plies (due to micro-buckling of fibers for 0° plies and to multiple shear micro-cracks for 90° plies) or within the plies as intra-laminar failure, fiber breakage, and matrix cracks (due to a combination of compression, bending, and shear)^{17,19} (Figure 2). The successive stages of composite tube progressive crushing have been well identified^{19,22,23} as displayed in Figure 3.

The localized fragmentation at the tip of the plies is pointed as the mechanism leading to the definition of the ply mean crushing stress (MCS),^{16,24} corresponding to a stable crushing level (Figure 3(f)), occurring after the yielding peak (Figure 3(b) and (c)) and stabilization phase (Figure 3(e)).

Most research works focus on means to increase the energy absorbed while reducing the initial peak load to enhance crushing performances. To that end, a multitude of factors have been studied.

The crashworthiness properties and energy absorption characteristics of structures with different cross-sectional shapes and geometries have been studied,²⁵ including in particular, sine-wave beams,^{10,13} semi-hexagonal specimens,²⁶ columns specimens,²⁷ conical shells²⁸⁻³⁰ or various tubular shapes,^{28,29,31,32} and corrugated tubes.^{28,29,33} Foremost, tubular shapes tested are circular^{1-3,5,7-9,12,14,18,20,28,29,34-48} or squared.^{5,18,28,29,39,42,45,49-55} Most studies find the energy absorption capability of squared tubular structures to be 0.5 times lower than that of circular ones. Tube scaling^{5,37} and especially the effect of thin-walled tubes and the influence of wall thickness^{14,21,25,27,30,46,51,52,54,56} have been considered, generally highlighting an energy absorption increase trend with the increase of the wall thickness.

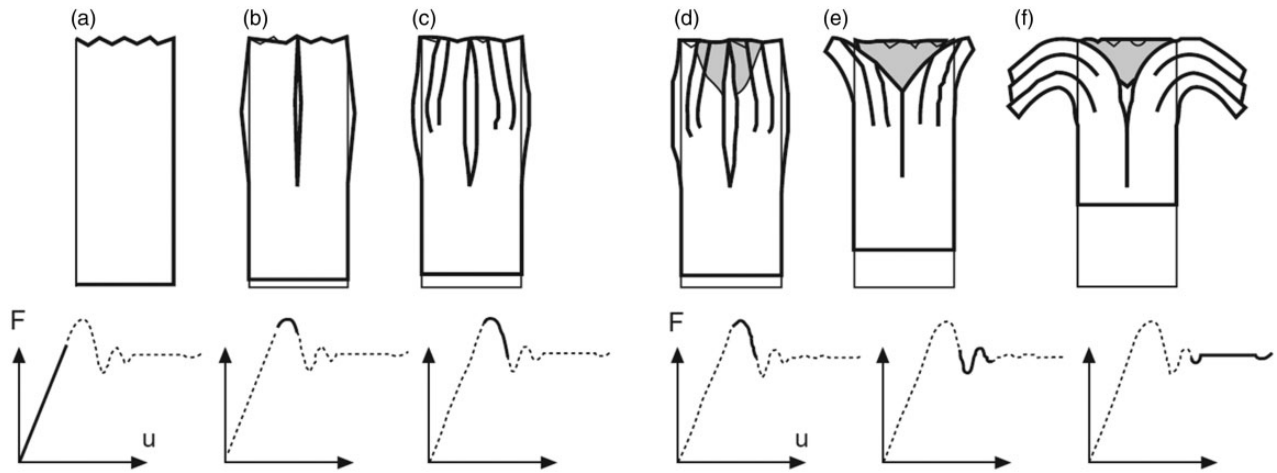


Figure 3. Consecutive crushing stages from Pinho et al.²²

Investigations have also been carried out on material's types used to manufacture the structures, mainly including carbon, glass, and aramid fibers, with a various range of polymeric resin:

Carbon,^{7,10,53} epoxy,^{2,5,8-14,16-18,20,21,32,33,35,36,38,39,41,46,50,57} PEEK,^{3,35,37,58} carbon/vinylester,^{39,45,51,52} carbon/polyamide,⁴³ glass/epoxy,^{10,12,18,30,33,40,47} E-glass/polyester,^{5,49,42,28,29,26} glass/vinylester,⁴² polypropylene,^{43,44} Kevlar/epoxy,^{1,5,8,9,18} hybrid materials,^{1,5} composite metal-fibers,^{25,54} hybrid aramid/carbon/epoxy,¹³ or even woven silk/epoxy.⁵⁵ Carruthers et al.⁵⁹ propose a review of the energy absorption capability and the crashworthiness of composite material and metal structures, giving values recorded for axially compressed FRP and metal tubes clearly highlighting the superiority of FRP structures over steel structures.

A comparison with steel and aluminum, with SEA values of 15 and 30 kJ.kg⁻¹, respectively,²¹ places FRP energy absorption capacity significantly above. Hamada et al.³⁵ report a value of 53 kJ.kg⁻¹ for $\pm 45^\circ$ -oriented carbon fibers/epoxy tubes while values range from 50 to 80 kJ.kg⁻¹ for a variety of glass fibers-reinforced thermosetting resin composites.³⁵ They also present a value of 110 kJ.kg⁻¹ obtained for carbon/epoxy tubes.¹⁹ This in accordance with Ramakrishna and Hull³⁶ reporting values of 85 to 120 kJ.kg⁻¹ for carbon/epoxy tubes [AQ2]. Those values are significantly below the 127 kJ.kg⁻¹ obtained for $\pm 30^\circ$ -oriented carbon fibers/PEEK tubes and the 180 kJ.kg⁻¹ obtained in the 0° carbon fibers/PEEK tubes.³⁵

The effect of fibers orientation,^{1,5,7,11-14,20,27,34,35,38-41,43,45,48,50-53,58} as well as the laminate stature, UD,^{5,7,11,13,16,17,28,29,32,41,47} 2D woven or braided structure^{7,21,26,28,29,33,36,39, 43,46,47,53,57} and

even triaxially braided composite tubes^{38,39,43-45,51,52} have also been tested in previous works. The relative amounts of 0° and 90° fibers as well as their position in the stratification of the tube's wall is a major factor that determines the geometry of the crush zone and therefore the specific energy absorption (SEA).³⁵

Similarly, previous works demonstrated that a fiber orientation along the axis of the composite tube absorbed more energy than other orientations.^{1,12,34} In that sense, many studies report a significant decrease of the energy absorption capacity with greater fiber orientation for carbon/epoxy tubes.^{12,38} Congruently, Chiu et al.³⁸ find that when varying the braided angle of composite laminate structures for composite tubes, the smallest braiding angles produce the highest SEA, up to 89 kJ.kg⁻¹ for a 20° angle (and 100 kJ.kg⁻¹ for 15° angle¹²) and reports a clear decline of the SEA value as the braiding angle increases, down by almost 50% to 45 kJ.kg⁻¹. Ramakrishna and Hull³⁶ conclude that the SEA capability increases with an appropriate fiber content and that the insertion of inlay fibers into the knitted fabric is an effective method of improving the energy absorption capability of fabric composite tubes.

Improving the crushing initiation with specific trigger geometries or profiles,⁴⁹ tulip shape,⁵⁵ notched out-lines,^{1,29,42} different tapered angles,⁴⁷ SMA trigger (shape memory alloy wires),⁴¹ inserting lateral circular cutouts⁵⁶ or by chamfering or beveling the edge,^{1,3,7,14,16-21,26,28,29,32,34-38,42,51} or using a double-chamfer trigger (chamfered at both ends)⁴⁰ has been attempted. The use of plug initiators^{21,39,45,46,51-53} is also a recurring attempt to initiate and enhance the crushing. Finally, specific boundary conditions with chamfer external triggers⁴⁶ or semi-circular cavity external trigger⁴⁶ have recently been tested. Tong and Xu⁴⁶ state that the energy absorption is improved by

53% by replacing a chamfer trigger with innovative trigger, with values ranging from 45 up to 102 kJ.kg⁻¹ for 2D-braided carbon/epoxy tubes.

To jump over the main points, two significantly exploitable axes of interest are standing out from the literature: materials and fibers orientation choice on one hand and trigger initiation and boundary conditions optimization on the other. These are the two aspects presented in this study (Part A and Part B).

The present study will relate to the experimental testing results of several circular composite tubes of different compositions and stratification. More specifically various combinations of unidirectional and woven structures as well as hybrid carbon–aramid reinforcement fibers are being tested. A first part will focus on the effect of different stratification and materials in a simple free-face crushing configuration between two compressive planes (Part A). A second part will present the effect of different trigger initiation systems on the crushing performances using mainly one singular sample, before highlighting specific features for each tube sample in some of the configurations (Part B). The work presented in this study therefore aims at

comparing the results in energy absorption capability of hybrid composite circular structures with different fibers orientations and of different natures (UD, woven) using specific boundary conditions and trigger initiation systems.

Experimental testing

Specimens and materials

A variety of fiber/epoxy tubes was acquired for testing, with different fibers orientations and fibers types. These fiber-reinforced tubular structures were studied in axial compressive crushing. In total, five specimens with different structures and different compositions were tested in various crushing configurations. Structural and material basis for the specimens include 12K HR carbon fibers and polymer epoxy resin. Fibers orientation and laminate stratification differ from one specimen to another as shown in Figures 4 and 5 and summarized in Table 1. Provided, tubular structures were machined and shaped in tubes of 100 mm length as pictured in Figure 4. Medium diameter was set at an

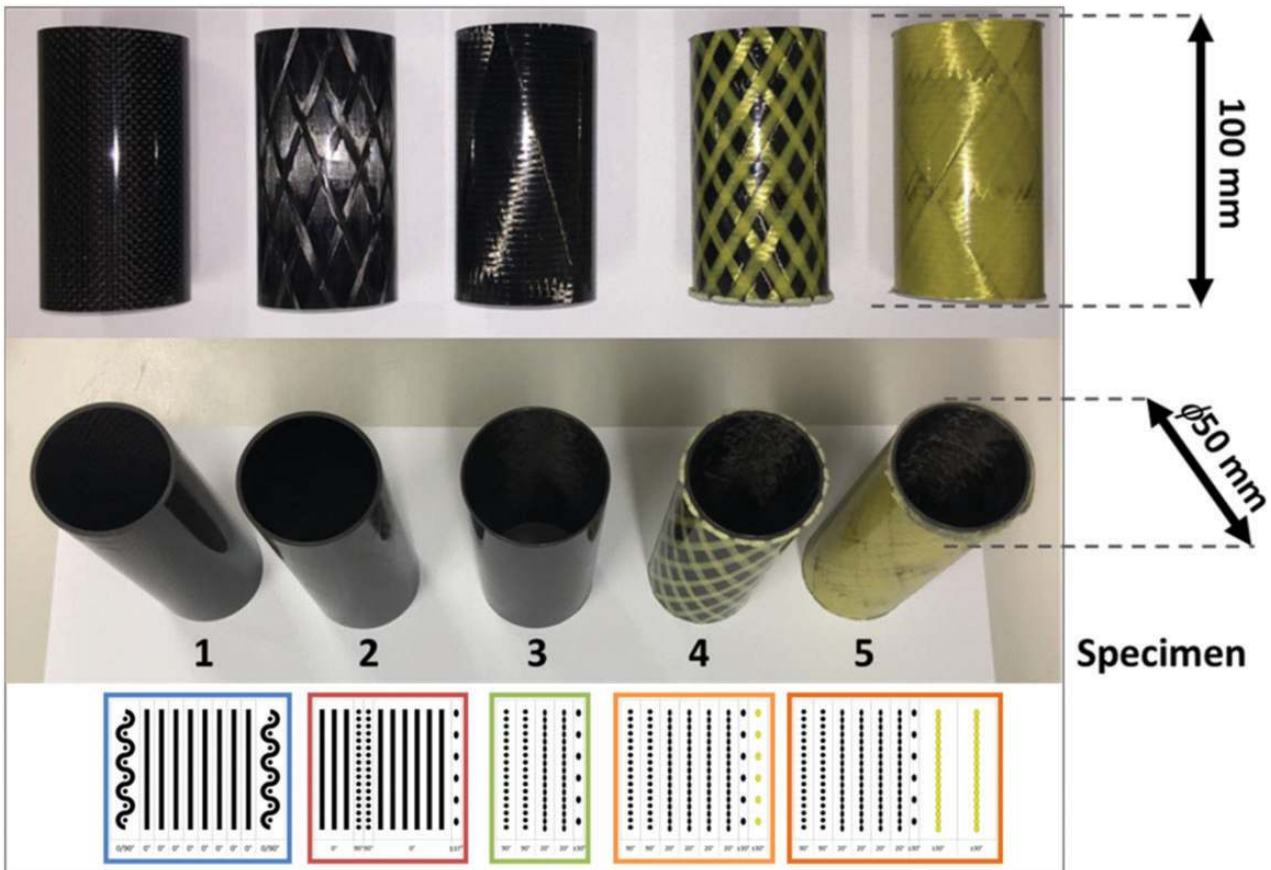


Figure 4. Picture of the five tube specimens with dimensions.

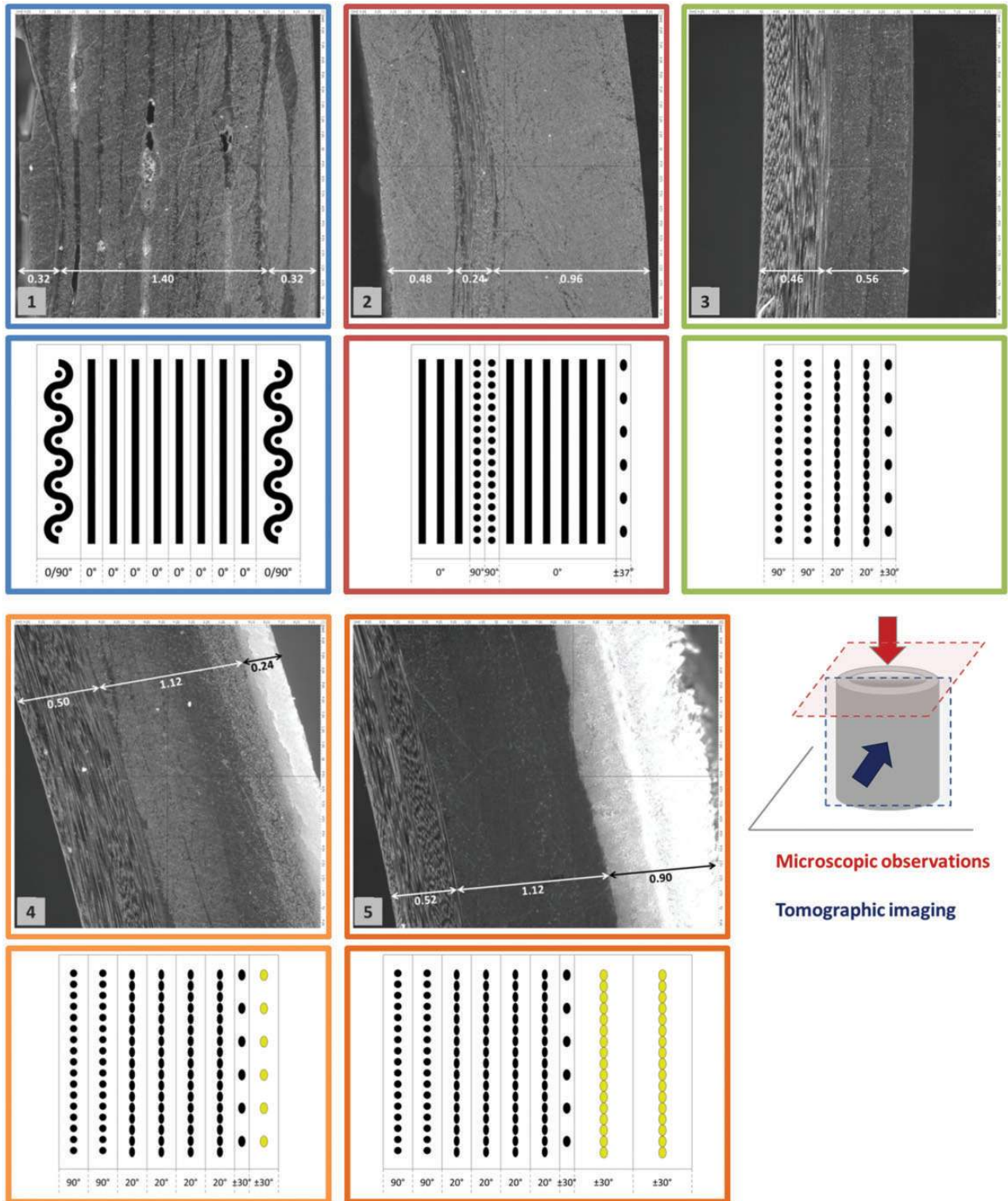


Figure 5. Microscopic observations of the five specimens section and corresponding schematic representations with their stratification.

average of 50 mm, with inner diameter varying from one sample to another due to stacking differences. Stratification layout and tube wall thickness are summarized in Table 1 for each sample.

The carbon/epoxy combination was selected with epoxy resin as a matrix because of its low density and for its high strength and good mechanical properties with reliable chemical stability, as well as its worthy

Table 1. Tube specimens' stratifications and properties.

| Ply—tube | Specimen 1 | Specimen 2 | Specimen 3 | Specimen 4 | Specimen 5 |
|-------------------------------|------------------------|------------------------|------------------------|-----------------------|------------------------|
| 1—Inner | 0/90° weave | C 0° | C 90° | C 90° | C 90° |
| 2 | 0° | C 90° | C 90° | C 90° | C 90° |
| 3 | 0° | C 90° | C 20° | C 20° | C 20° |
| 4 | 0° | C 0° | C 20° | C 20° | C 20° |
| 5 | 0° | C ±37° weave | C ±30° weave | C 20° | C 20° |
| 6 | 0° | C | | 20° | C 20° |
| 7 | 0° | C | | ±30° weave | C ±30° weave |
| 8 | 0° | C | | ±30° weave | A ±30° weave |
| 9 | 0° | C | | (30% cover) | ±30° weave |
| 10—Outer | 0/90° weave | C | | | (100% cover) |
| Wall thickness (mm) | 2 | 1.8 | 1.1 | 1.85 | 2.45 |
| Int. diameter (mm) | 46 | 46.5 | 50 | 45 | 45 |
| Ext. diameter (mm) | 50 | 50 | 52 | 48.5 | 49.5 |
| Density (kg.m ⁻³) | 1.34 × 10 ³ | 1.69 × 10 ³ | 1.43 × 10 ³ | 1.5 × 10 ³ | 1.39 × 10 ³ |

C: carbon; A: aramid.

performance regarding energy absorption based on the literature review and due to the aeronautical context.

In order to verify and establish the composition and stratification of the composite tube specimens, samples were polished and observed using a high-resolution optical microscope. Measurements and images acquisitions were performed using an Alicona Infinite Focus SL microscope system with a 10× to 50× magnification. Resulting observations are displayed in Figure 5, along with a lay-up schematization.

For the laminate lay-up schematization presented in Figure 5, the 0° direction of the fibers was chosen to coincide with the longitudinal axis of the tube and subsequently with the axial crushing direction. Plies dimensions are given as an averaged best approximation since plies thickness is not even and regular. That is supposedly the results of the fabrication process.

Table 1 reports the structural specificities and geometrical properties for the five tube specimens.

When looking at the density values from Table 1, it can be pointed out that they are relatively low for some samples (sample 1 especially, and to a lesser extent, sample 3). This is allegedly strongly related to the high porosity observed in the samples (Figure 5) and also lower fiber density (or fraction volume v_f) in some areas of the samples.

Table 2 intends a comparison in stiffness and compressive strength failure between experimentally and theoretically obtained values for all five samples. Both the experimental and theoretical methods used to achieve those results are presented below. The magnitude referred to as stiffness (in MPa) relates to the elastic compressive modulus (Young's modulus).

Table 2. Stiffness and compressive strength properties for tube sample stratifications.

| | Experimental methods | | | | Theoretical methods | |
|--------|----------------------|----------------------------|------|-----------------|----------------------------|------|
| | Stiffness (MPa) | Compressive strength (MPa) | | Stiffness (MPa) | Compressive strength (MPa) | |
| Tube 1 | 43,700 | +2800 | -350 | +100 | 54,200 | -650 |
| | | -5200 | | -139 | | |
| Tube 2 | 54,300 | +4900 | -340 | +65 | 52,100 | -652 |
| | | -3100 | | -102 | | |
| Tube 3 | 30,200 | +8700 | -170 | +47 | 22,800 | -265 |
| | | -8600 | | -92 | | |
| Tube 4 | 27,300 | +6800 | -180 | +44 | 24,500 | -259 |
| | | -6000 | | -59 | | |
| Tube 5 | 24,700 | +3600 | -200 | +29 | 23,600 | -250 |
| | | -5400 | | -41 | | |
| Tube 1 | 43,700 | +2800 | 350 | +100 | 54,200 | 650 |
| | | -5200 | | -139 | | |
| Tube 2 | 54,300 | +4900 | 340 | +65 | 52,100 | 652 |
| | | -3100 | | -102 | | |
| Tube 3 | 30,200 | +8700 | 170 | +47 | 22,800 | 265 |
| | | -8600 | | -92 | | |
| Tube 4 | 27,300 | +6800 | 180 | +44 | 24,500 | 259 |
| | | -6000 | | -59 | | |
| Tube 5 | 24,700 | +3600 | 200 | +29 | 23,600 | 250 |
| | | -5400 | | -41 | | |

For the five tubular specimens (and especially for tube samples 1 and 2), materials and fibers properties are not well known and identified nor completely mastered. Compressive experimental testing shows that fibers mechanical properties are less resistant than

usually encountered in current modern composite materials.

In order to better estimate the mechanical properties of the materials used to manufacture these samples and to correlate the theoretical and experimental stiffness, Classical Lamination Theory was used. Taking a failure criterion expressed in fibers compression strain, chosen at $\epsilon_{failure} = -0.0125$ (a typical value for carbon fiber²⁴) for all the plies, an estimated stress failure value was calculated for each sample, for the first ply reaching $\epsilon_{failure}$, and reported in Table 2. This calculation was done in order to roughly evaluate the mechanical properties and should be taken with caution. For the woven plies of the structures, mechanical properties were also calculated using the Classical Lamination Theory, but the related plies were approximated as two superposed oriented unidirectional plies of half the thickness. The mechanical stiffness properties used for the theoretical calculations with the Classical Lamination Theory are reported in Table 3, where E_l is the longitudinal

modulus, E_t the transverse modulus, G_{lt} the shear modulus, and ν_{lt} Poisson's ratio.

When comparing values from the theoretical calculations to the experimental data (Table 2), the latter reflects lower values in stress failure, although it can be noted that they remain in the same order of magnitude. Besides, the experimental compressive strength values that are reported in Table 2 are rather related to a failure in crushing mode than pure compression.

Figure 6 presents the experimental mechanical stiffness modulus obtained from quasi-static axial compression testing of samples 1 to 5 positioned under two crushing plane, used as a free-crushing face for the bottom plane and being slightly encased on top for the upper plane, to avoid drifting. Actual testing begins with the tube structure in contact at both ends and being very slightly stress loaded.

Those compression tests were performed on each sample along the axial direction, and a compression stiffness modulus was experimentally evaluated while the materials remained in their elastic deformation, as presented in Figure 6 and reported in Table 2.

Results reported in Table 2 show that the compression stiffness is lower than anticipated for three of the five CFRP specimens, especially for specimens 1 and 3. Compression failure is also lower than estimated, especially for specimens 1 and 2 that incidentally mainly present 0° -oriented fibers.

This supports the hypothesis of poor fibers' properties used to manufacture the tubular specimens, and it can also be explained by the high porosity inherent to many samples, as observed on the microscopic images (Figure 5). This is also most obvious for tube

Table 3. Mechanical properties used for the Classical Lamination Theory calculations.

| | E_l (MPa) | E_t (MPa) | G_{lt} (MPa) | ν_{lt} |
|--------|-------------|-------------|----------------|------------|
| Carbon | | | | |
| UD | 62,000 | 7700 | 4200 | 0.25 |
| Woven | 35,000 | 35,000 | 4200 | 0.05 |
| Aramid | | | | |
| UD | 61,000 | 4200 | 2900 | 0.35 |
| Woven | 30,000 | 30,000 | 2900 | 0.30 |

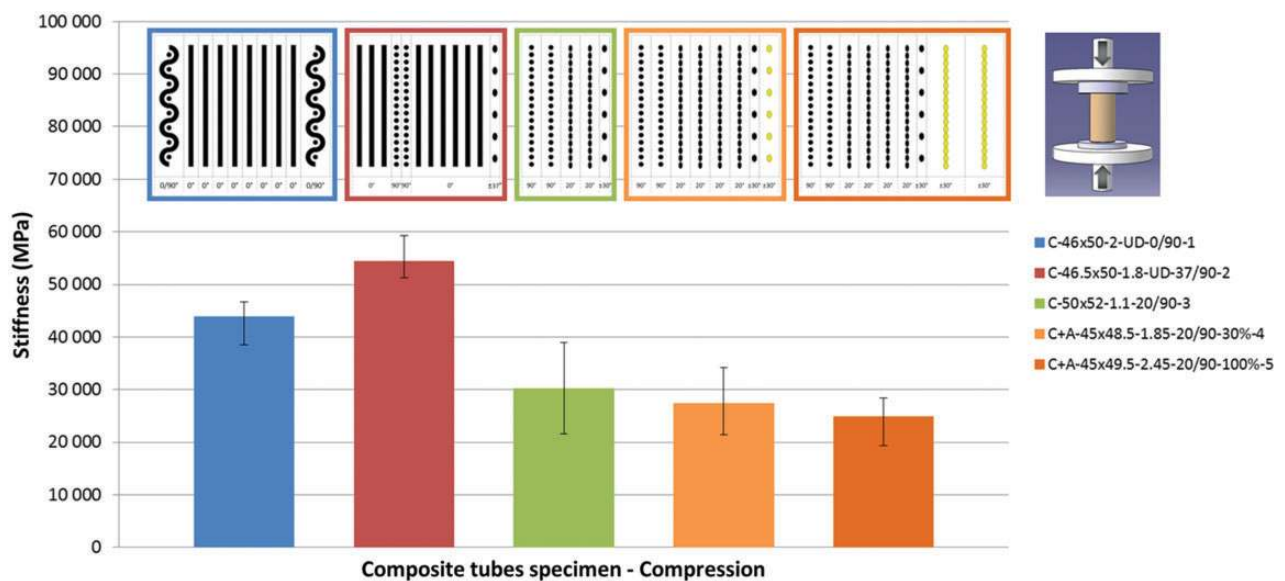


Figure 6. Compression stiffness from experimental testing of axial crushing for tubes 1 to 5.

specimen 1, for which braided thread remnants from the manufacturing process are visible too. In addition, experimental compressive failure values resulting from the performed compression tests could rather be affected by a bearing phenomenon under the tip of the plies and resulting from the crushing nature of the solicitation than related to a pure compressive mode; hence, the observed discrepancy in compression strength failure, which thereafter seems more rational.

Test set-up and configurations

Quasi-static crushing tests were carried out using a 250 kN Schenck hydraulic testing machine in compression testing mode, through a constant loading speed of $0.2 \text{ mm}\cdot\text{s}^{-1}$ (Figure 7). To account for reproducibility, tube specimens were tested at least three to five times on average (and up to 10 times) for each sample and each configuration.

Experimental results

Part A: Material effect

This first part presents the experimental results for the free face axial compressive crushing of the five CFRP circular tubes mentioned above between two plane surfaces.

Figure 8 represents the stress–displacement curve resulting from such trials, for tube specimen 1. The stress thereby represented corresponds to an average value from multiple trials for the same specimen and the same testing configuration, with the dispersion

range indicated on both sides of the curve, corresponding to the minimum and maximum stress value for all trials for each displacement value.

Generally it can be noted a relatively good repeatability in the trials, especially for composite material, with a dispersion averaging -12% and $+32\%$, compared to the medium value, as illustrated in Figure 8. Overall, less than 2% of the total of tested samples has been discarded for being deemed aberrant.

A crushing curve such as the ones displayed in Figures 8 and 1 can be divided into three main parts: a loading phase ending by the main rupture of the structure and leading to a peak, a stabilization phase, and a stable crushing phase.^{19,23} Sometimes, when crushing is extended long enough, a last phase known as compaction of debris or densification may occur, matching an increase of the end of the curve.

Once reached, the level of the crushing threshold or MCS^{16,24} is very steady and regular from one trial to another. The compression stiffness is also mainly identical from one trial to another. However, it can be observed a large dispersion on the peak value itself, with random values being reached before a structure failure.

In practical terms, this uncontrolled dispersion on the crushing peak and its higher values are unwanted for a crash absorption system, as it produces important accelerations for the structure and therefore the passengers. With this standpoint in consideration, several configurations and crushing initiations have been tested in order to limit this main peak.

Apart from the multitude of resin and fibers debris generated during crushing, splaying (both inward and outward) and large bands of material resulting from

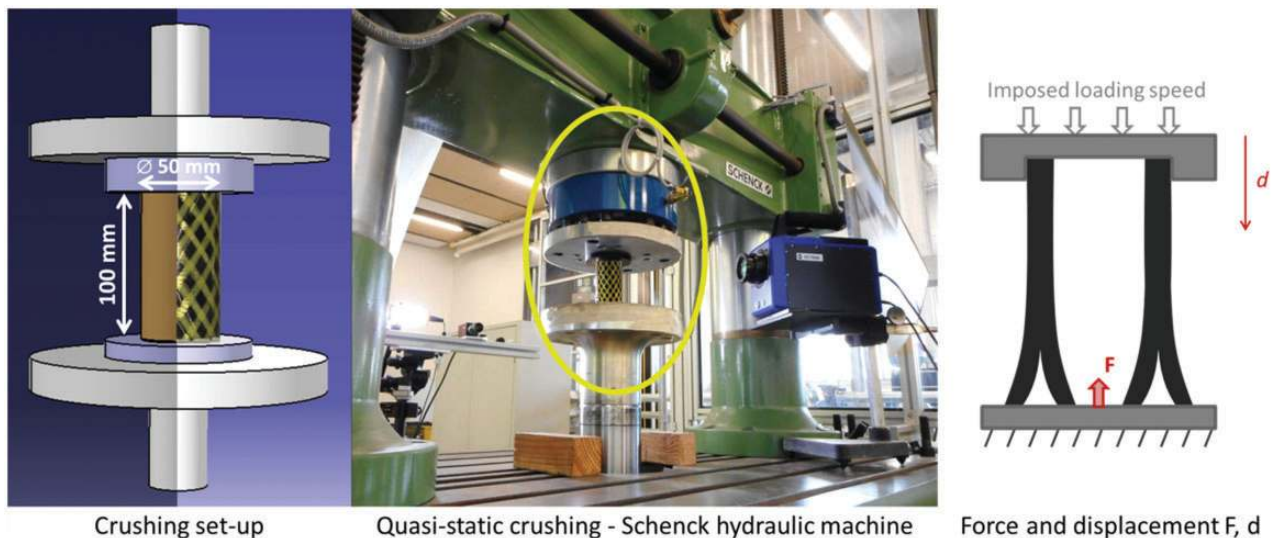


Figure 7. Quasi-static crushing test set-up and equipment.

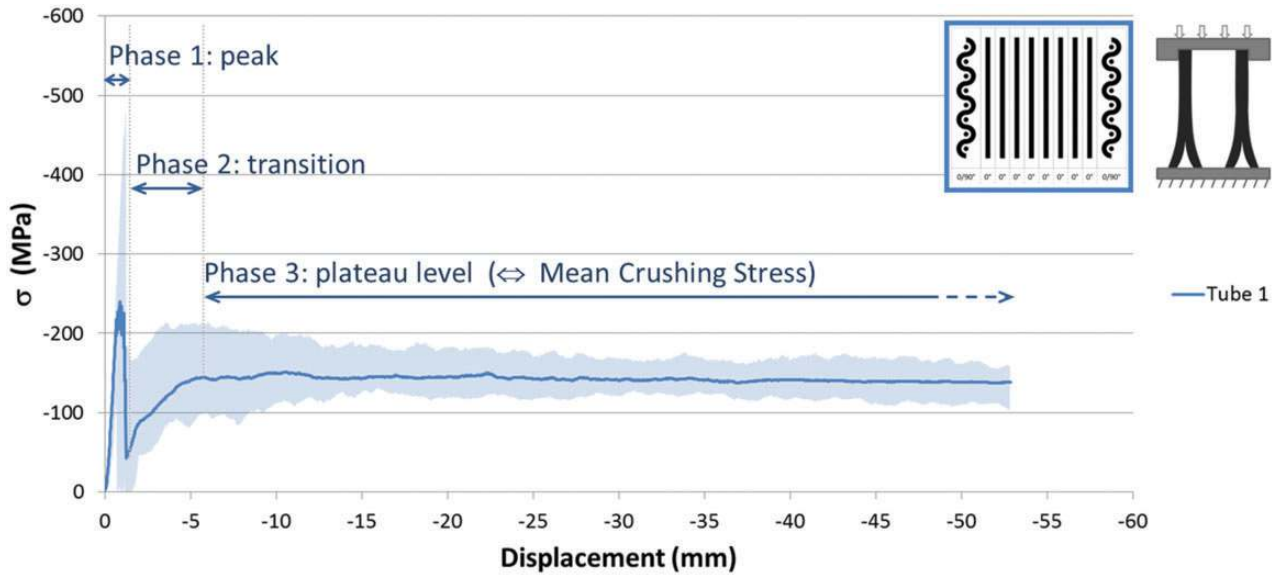


Figure 8. Stress–displacement curve and dispersion for tube 1, resulting from 10 trials.

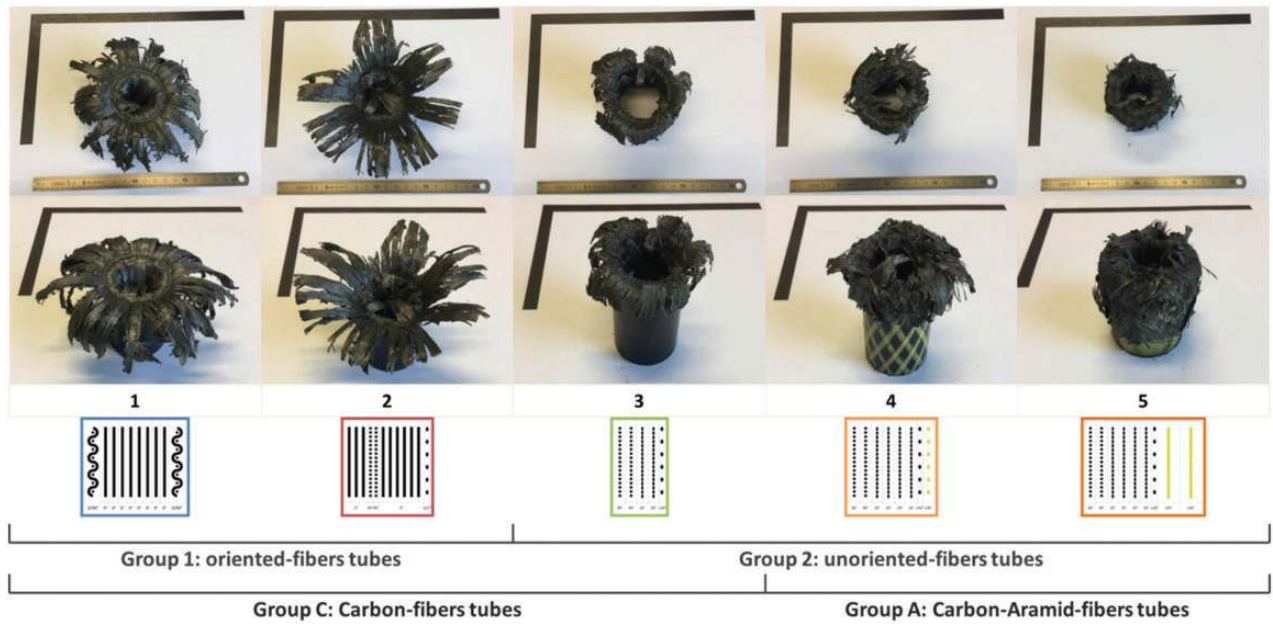


Figure 9. Crushed CFRP tube specimens 1 to 5, from the top (above) and from the side (below).

intra-laminar shear are a consequence of composite laminate crushing, as seen on picture in Figure 9.

A difference can be observed between tubes samples 1 and 2 presenting both inner and outer spreading of splayed parts and tubes samples 3, 4, and 5 mainly presenting outer spreading. This can be explained mostly by the core structure of the tubular samples, with oriented fibers pattern (specimens 1 and 2) and unoriented fibers pattern (specimens 3, 4, and 5).

Additionally, a specificity can be mentioned for samples with an aramid overlayer (tube specimens 4 and 5) as this latter acts as a girdle, drawing the shattered composite parts, resulting in a closer folding and wrapping around itself.

Figure 10 gives the load over the axial displacement curves for the five tube specimens in axial crushing. It can be noted that after the initial load peak (corresponding to the structure yield) has passed and once

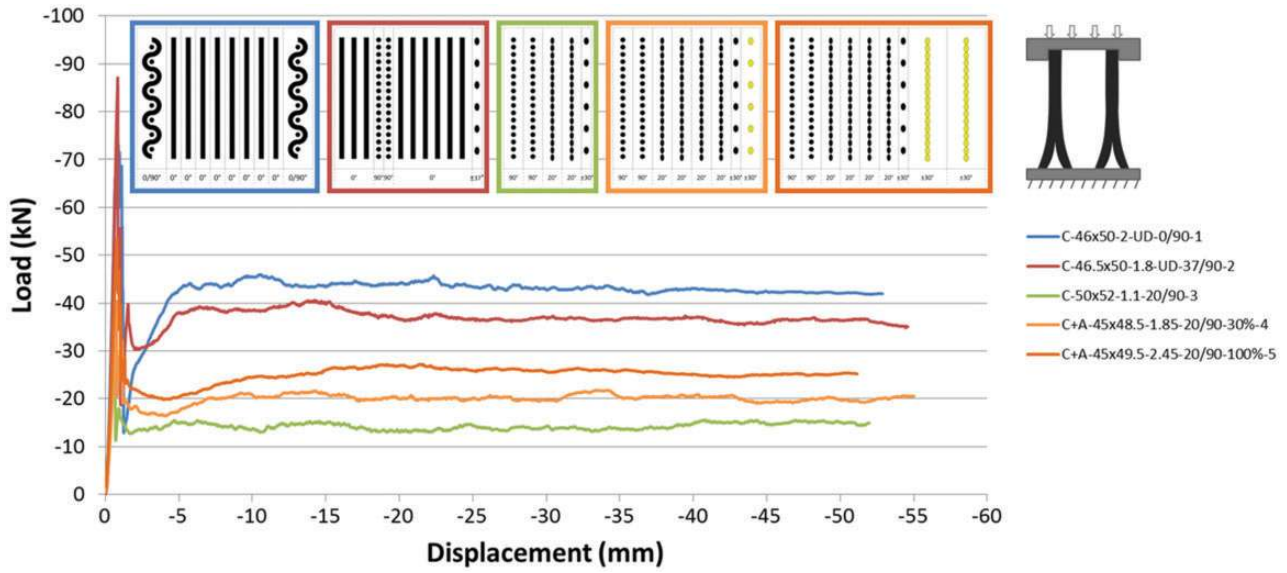


Figure 10. Load–displacement curves of axial crushing of tubes 1 to 5.

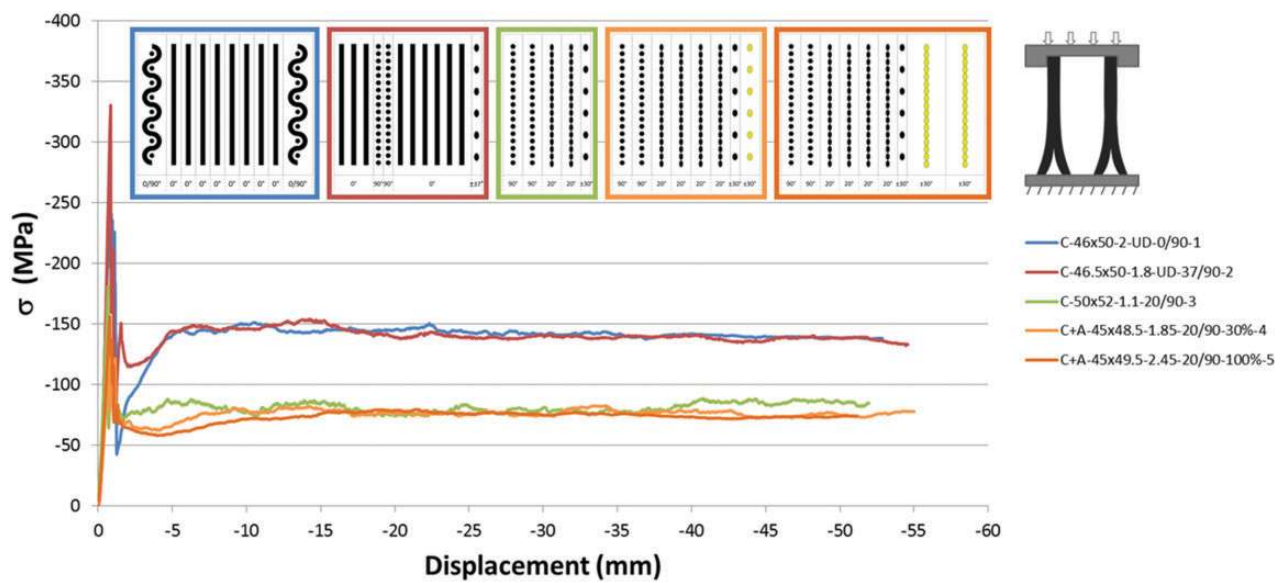


Figure 11. Stress–displacement curves of axial crushing of tubes 1 to 5.

the crushing phase has established and become constant, the range of crushing load varies from 15 kN to 40 kN.

Figure 11 presents the crushing stress over the axial displacement for the five tube specimens in axial crushing.

Two groups of CFRP tube specimens can be made from the stress–displacement curves resulting from axial compression, with tubes 1 and 2 averaging a higher value of nearly 140 MPa for the MCS plateau and tubes 3 to 5 lowering at 75 MPa. This is directly resulting from the structure and stratification of the

tube specimens, which can consequently be separated into two groups: group 1: oriented fibers tubes (tube specimens 1 and 2) and group 2: unoriented fibers tubes (tube specimens 3, 4, and 5).

Overall, this result seems rational as composite fibers need to be unidirectionally oriented in the loading direction (in this case, 0°) to return a maximal stress value. This is in accordance with previous studies.^{1,12,34–36,38} Nevertheless, some transversally oriented fibers are still required to stabilize the whole structure, as it is the case for tube specimen 1, where the woven pattern for the upper and lower ply is present to stabilize the

unidirectional core and which coincidentally happens to be the strongest sample.

Finally, it can be noted that the length of the stabilization phase is directly linked to the wall thickness of the tube specimens; it corresponds to approximately twice the thickness (Figure 11, Table 1).

One means to characterize and compare the absorbing capability of materials is through the SEA, also referred to as specific sustained crush stress. The SEA value is given by the following equation

$$SEA = \frac{EA}{m} = \frac{1}{\rho \cdot u} \int_0^u \sigma(u^*) du^* \quad (1)$$

where EA is the energy absorbed (given by the area under the force–displacement curve), divided by the mass of the crushed mater m, σ is the compression stress, u the crushing distance, and ρ the density of the material.

It can be established that the SEA value can be very closely approximated as an instantaneous value using the crushing stress σ_{cr} divided by the density ρ of the crushed material (equation (2))

$$SEA \xrightarrow{\sigma \rightarrow const} \frac{\sigma_{cr}}{\rho} \quad (2)$$

Although displaying a similar stress level value for the MSC plateau (Figure 11), when related to their respective density, tubes 1 and 2 differ greatly in term of absorption capability (Figure 12), with tube 1 presenting an average of 110 kJ.kg^{-1} and tube 2 of

80 kJ.kg^{-1} while the second group of specimens show lower values, near 55 kJ.kg^{-1} .

Similarity in behavior and energy absorbing capability for specimens 3, 4, and 5 are not incoherent when referring to Table 1, which shows the same basis structure for those specimens. Outer aramid covering does not improve or worsen the general behavior or energy absorbing capability.

Once the transition phase has passed, the SEA value tends toward a constant value, as displayed in Figure 13. The influence of the peak can be noticed at the very beginning of the curve and a displacement of at least 10 mm is needed to erase the effect of this peak.

The histogram chart shown in Figure 14 displays the average SEA values for each tube sample in free axial crushing. They are presented side-by-side with a factor, referred to as overshoot, and defined by the crushing stress initial peak maximum value divided by the density (equation (3)). This indicator was chosen to represent and compare the overflow of energy for each sample

$$\text{Overshoot} = \frac{\sigma_{max}}{\rho} \quad (3)$$

As the overshoot is uniform to the SEA (kJ.kg^{-1}), a direct comparison between these two values is possible, and it can be revealed that for each specimen, the overshoot is at least twice as high as the SEA value ($\times 2$ for tube specimen 3, $\times 2.5$ for tube specimen 1, and up to $\times 2.8$ for tube specimen 5).

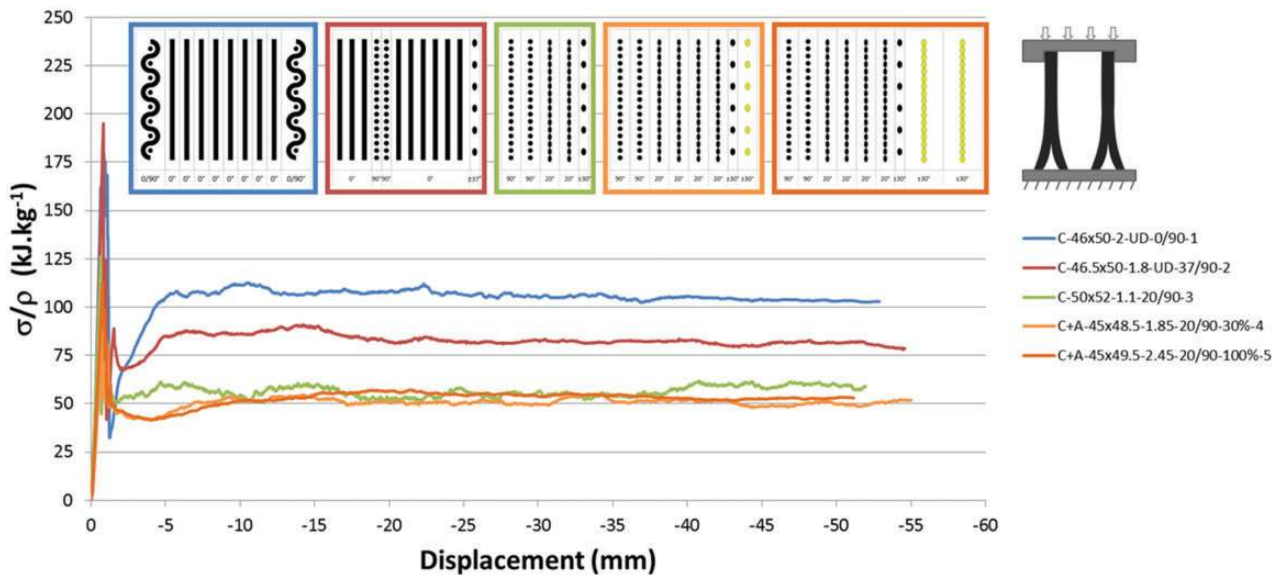


Figure 12. Stress/density over displacement curves of experimental crushing for tubes 1 to 5.

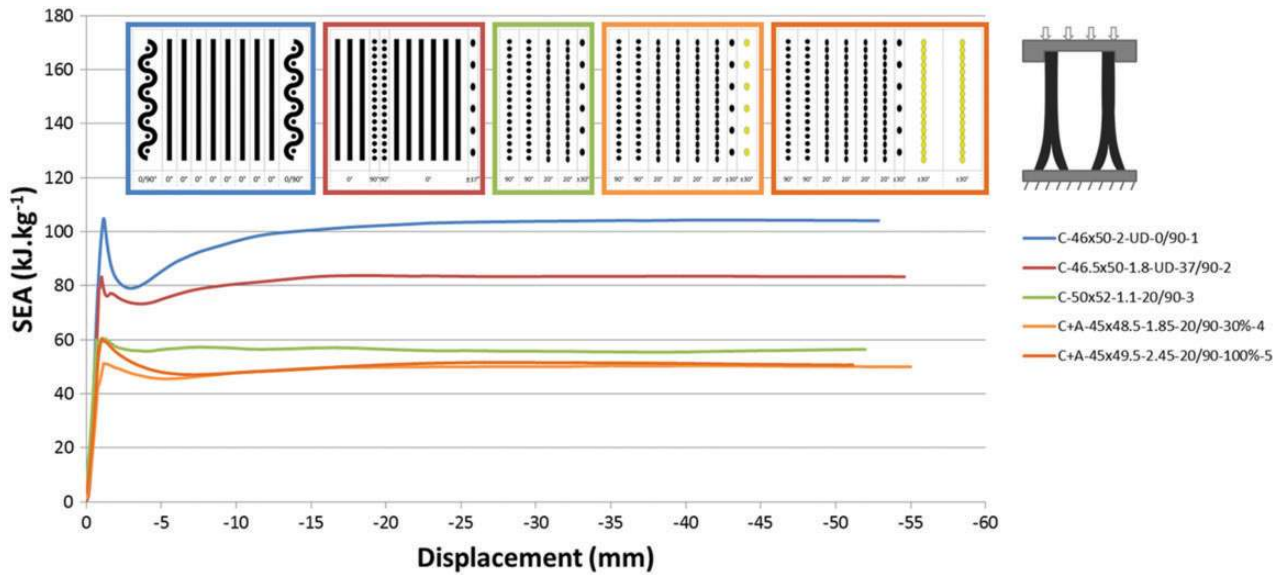


Figure 13. SEA evolution for five CFRP tube specimens submitted to pure axial crushing.

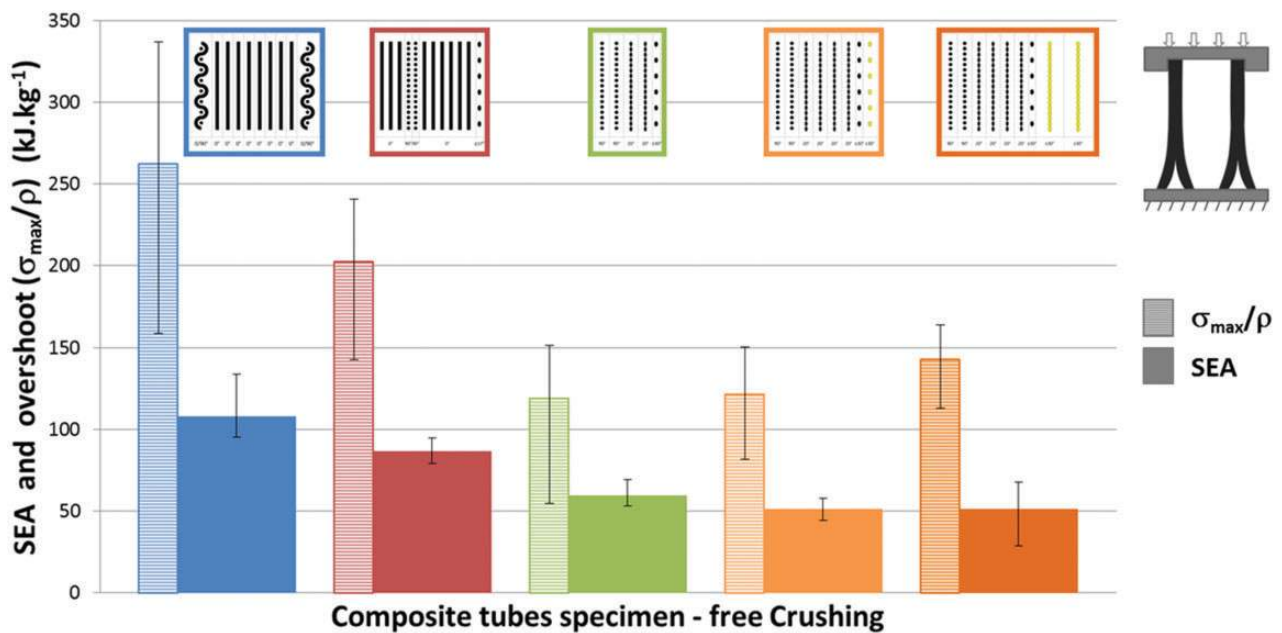


Figure 14. SEA values for five CFRP tubes submitted to pure axial crushing and overshoot value.

Some instances in the literature refer to the *Load Uniformity* or *Trigger Ratio* defined as F_{max}/F_{mean} or *Crushing Load Efficiency* defined as F_{mean}/F_{max} .⁴⁸ The overshoot parameter was deemed more suited to represent the overflow of energy than the other parameters or ratios from the literature. Furthermore, as it is homogenous to the SEA, the comparison between the two magnitudes is made easier.

In order to limit the peak and therefore reduce the overshoot, several boundary conditions and crushing initiations have been tested.

Intermediate conclusion

To summarize the first part of this experimental work, the following observations can be made:

1. Failure mechanisms remained similar for all tube samples, with moderate to significant splitting, delamination, and multiple brittle crack paths, leading to large debris creation.
2. Tubular specimens with 0° fibers oriented in the loading axial direction perform better in

- compressive strength and therefore return higher SEA values.
3. Woven fabric plies help containing and guiding the unidirectional plies, restraining them from splaying too easily.
 4. Aramid fibers bring no additional rigidity or energy dispersion capability, but aramid-covered tube samples contain the fragmented carbon/matrix wreckagees better, avoiding large spillage.

Part B: Configuration effect

Several configurations were tested for crushing initiation improvement and hopeful energy absorption enhancement. Tubular structures were clamped and encased at one end at the top, while several options were tested for the other end at the bottom. They were (a) let free on a plane surface, (b) also encased, (c) encased while guided through a conic shape, (d) positioned on a conic plug initiator, and (e) submitted to

pure flaring, where the structure gradually becomes wider from one end to the other, as a conic part passed through. Figure 15 presents the five configurations tested. The general motivation for each testing configuration was (a) to use a reference case, similar to what is found in the literature, (b) try and enhance the SEA value, (c) try and reduce the overshoot, (d) inversely to (c) test an outer dispersion, that could be compared to (a), and (e) with the later aiming at testing and evaluating the benefits of the crimping property alone.

For the two conic-shaped configurations ((c) and (d)), specific conic-shape parts were designed and machined for each specimens according to the specificity of each tube's internal diameters (Table 4), with a goal of expressing a hoop strain of $20,000 \mu\epsilon$ and $-15,000 \mu\epsilon$, respectively, via the gradual slope. Those values are usual approximations of tension and compression stain ruptures for composite materials. A detailed schematization (Figure 16) gives the diametric information that is reported in Table 4.

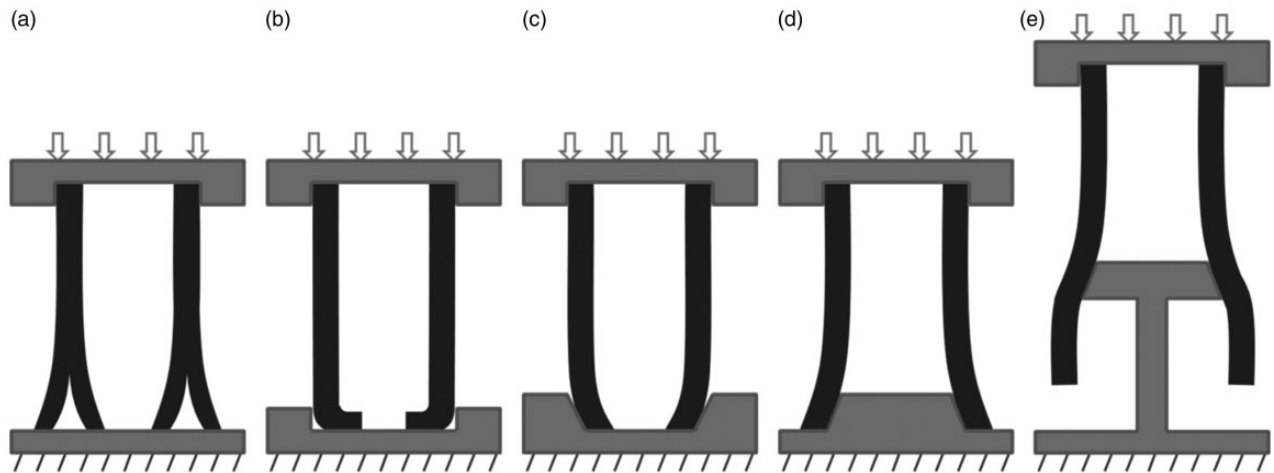


Figure 15. Experimental testing configurations (a) to (e). (a) Free crushing, (b) inner crushing, (c) inner conic crushing with sloping initiation, (d) outer conic crushing with plug initiation, and (e) pure plug flaring.

Table 4. Conic-shaped parts specifications and dimensions for inner and outer cones **[AQ3]**.

| Tube | Specimen 1 | Specimen 2 | Specimen 3 | Specimen 4 | Specimen 5 |
|-------------------------------------|--------------|--------------|--------------|--------------|--------------|
| Int. diameter (mm) | 46 | 46.5 | 50 | 45 | 45 |
| Ext. diameter (mm) | 50 | 50 | 52 | 48.5 | 49.5 |
| Outer cone ($20,000 \mu\epsilon$) | Outer cone 1 | Outer cone 2 | Outer cone 3 | Outer cone 4 | Outer cone 5 |
| Outer cone d_{int} (mm) | 44 | 44.6 | 47.9 | 43 | 43 |
| Outer cone D_{int} (mm) | 46.9 | 47.5 | 50.9 | 45.9 | 45.9 |
| Inner cone ($15,000 \mu\epsilon$) | Inner cone 1 | Inner cone 2 | Inner cone 3 | Inner cone 4 | Inner cone 5 |
| Inner cone D_{ext} (mm) | 52 | 52 | 54 | 50.5 | 51.5 |
| Inner cone d_{ext} (mm) | 49.3 | 49.3 | 51.2 | 47.8 | 48.8 |

For the outer cone (forcing a hoop strain of 0.020), the diameter of the base of the conic part (D_{int}) was made to match the interior diameter (int. diam.) of the tube and for the inner cone (forcing a compressive hoop strain of -0.015), the diameter of the base of the conic-shaped part (d_{ext}) was made to match the exterior diameter (ext. diam.) of the tube. Specifications are reported in Table 4.

As an illustration, the pictures in Figure 17 present the difference in crushing behavior for the same CFRP tube specimen (tube 1) submitted to axial crushing under the first two configurations ((a) and (b)) presented in Figure 15. Both underwent progressive crushing. The first (left) corresponding to configuration type (a) presents both inner and outer spreading of splayed parts, whereas the second (right) corresponding to configuration type (b) reveals the whole bundle of splayed parts folding towards the inside of the tube.

Configuration type (d), with a cone-shaped plug initiator, does not differ much from configuration type (a)

apart from the fact that the entire splayed bundle spreads on the outside and configuration type (c), with an inner-conic-shaped part, does not differ from configuration (b). This can also be correlated by the tomographic images.

Figure 18 displays the stress/density over displacement results for tube specimen 1, for the 5 described configurations. In case of inner-crushing confinement (b), a slight but still significant increase of the curve can be noted towards the end, starting at 40 mm (↓). This rise should even be starting sooner, at about 23 mm (half the tube's interior diameter; (+)), when the wall's inferior end meets at the center of the tube (Figure 19).

Surprisingly, this outcome is not seen for configuration (c, inner conic crushing) where the end of the tube's wall also meets at the center. This might be explained by the fact that the tube's wall's ends are too damaged or too much fractured by the friction and the progressive confinement induced by the conic sloped part.

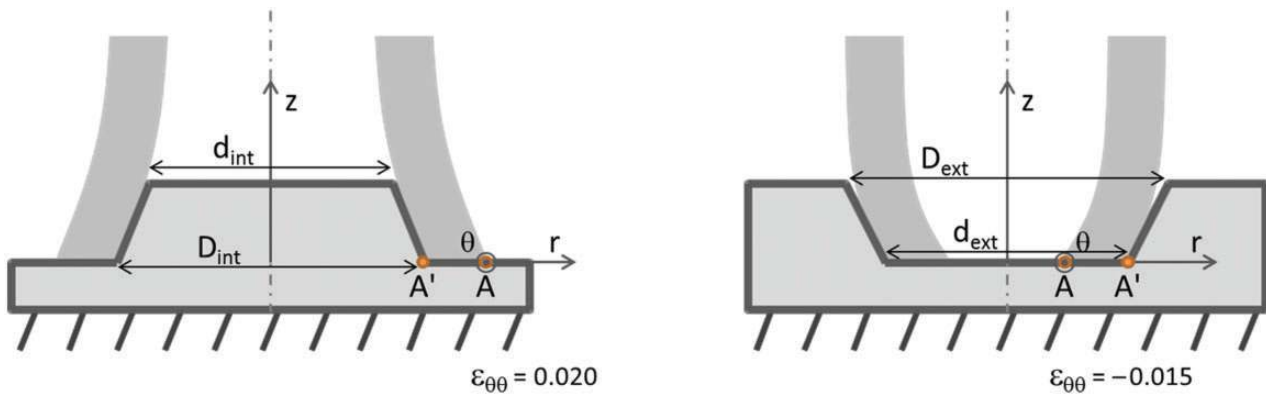


Figure 16. Outer (left) and Inner (right) conic-shaped parts used to change the boundary conditions.

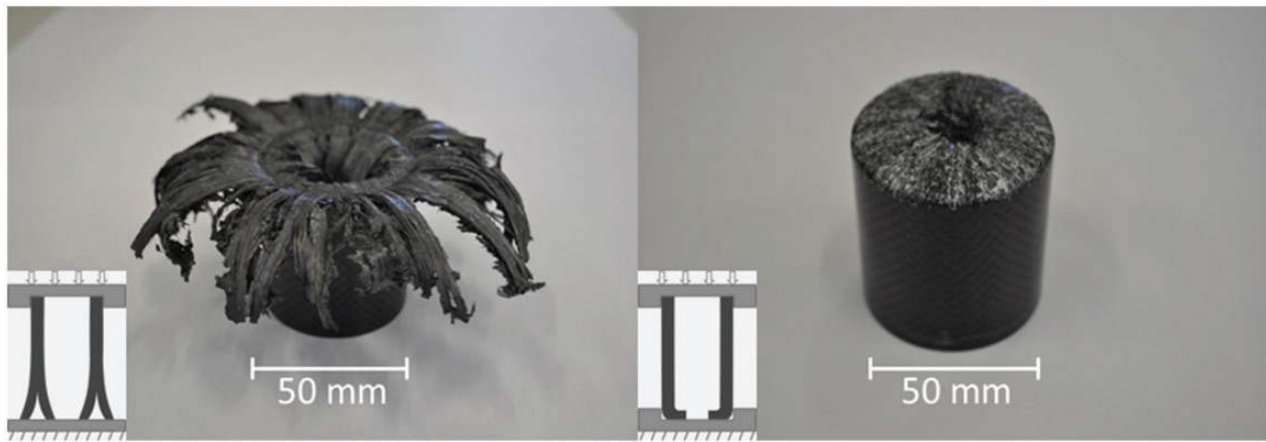


Figure 17. Crushed CFRP tube I showing outer spreading (left) and inner folding (right) based on boundary condition (a) free crushing and (b) inner crushing, respectively.

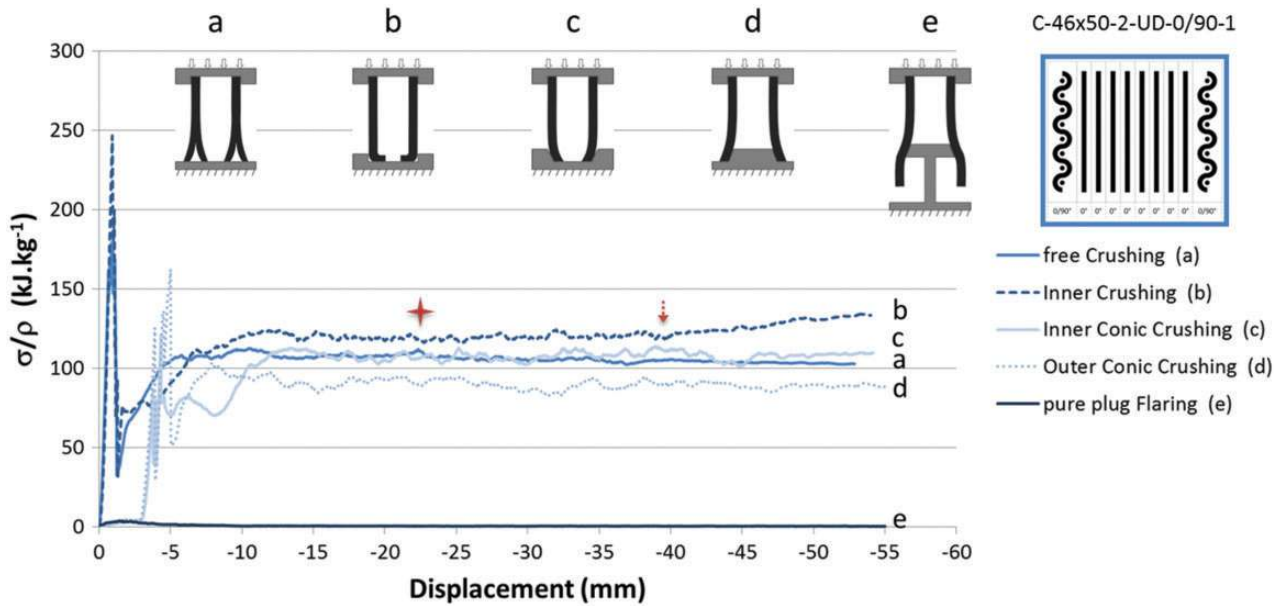


Figure 18. Stress/density over displacement curves of experimental crushing for tube specimen I submitted to axial crushing under five configurations.

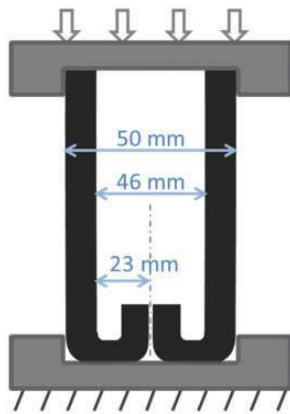


Figure 19. Schematic representation of the tube's wall convergence and collision, for the inner-crushing configuration (with tube specimen I dimensions).

This increase of the stress at the end could be beneficial and valuable for a surge in the SEA value: the densification of partially crushed material inside the tubular structure stabilizes the crushing process, resulting in an increase of the MCS and therefore the SEA.

For configurations with a conic initiation (inner or outer), (c) and (d), respectively, hoop stress is first generated, and axial crushing force takes longer to apply as the interior diameter of the tubular structure slides along the conic slope, before being axially loaded, as can be seen in Figure 18 for configurations (c) and (d), between 0 and 3 mm displacement.

The very beginning of the stress–displacement curve for those two configurations matches the last configuration (e), where the conic-shaped plug widens the extremity of the tubular structure. This setback is incidental to the height of the conic shape (δ , Figures 16 and 20).

Pure flaring (configuration (e)) was tested to try and take advantage of the crimping property of woven structures in braided composite tubes (Figure 21). Furthermore, the idea was to compare configuration (d) with configurations (a) and (e) and evaluate if the total energy dissipated by (d) was the summation of (a) and (e). Needless to say when referring to Figure 18 that this is hardly the case, with configuration (e) only dissipating 1 or 2% of the energy compared to pure axial crushing (configuration (a)).

In braided or woven patterns, the crimping can be characterized by the ratio of the real length of the fully deployed fiber (B) divided by the actual length of this fiber within the woven pattern (A, Figure 21 and equation (4))

$$\text{Crimping} = \frac{B_{\text{length}} \times 100}{A_{\text{length}}} \quad (4)$$

Overall, although trying to make the most of the crimping configuration in woven patterns seemed promising and worth investigating, this attempt unfortunately proved to be unpractical and non-optimal in terms of energy dissipation afterwards.

The histogram chart shown in Figure 22 displays the average SEA values side-by-side with the overshoot for

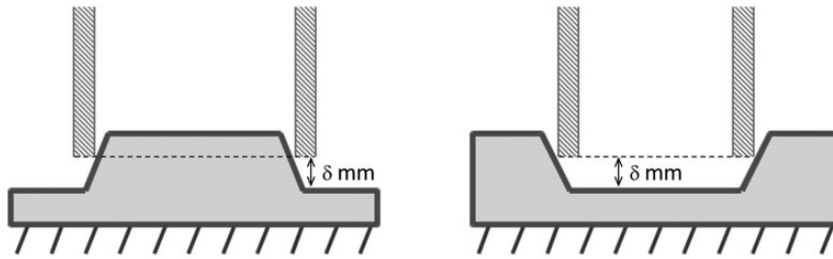


Figure 20. Outer and inner conic parts and initial tube position.

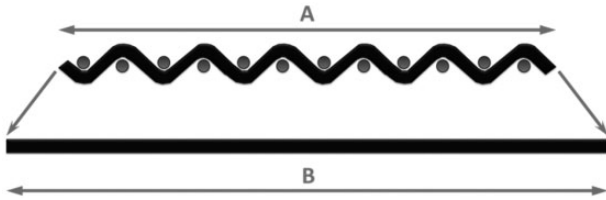


Figure 21. Crimping schematization.

tube specimen 1 for the five crushing configurations. Although the SEA remains in the same range for the first four configurations, with configuration (b, inner crushing) being slightly greater, the overshoot (σ_{\max}/ρ) presents more disparities.

For each axial compression tests, a stiff peak can be observed on the stress/density–displacement curves as showed in Figure 18, when the structure yields before it starts collapsing by progressive crushing at a stable and constant stress, as reflected by the continuous plateau value. Ideally, the gap between the peak and plateau value has to be reduced to a minimum, as a small gap and constant plateau level means an optimized dissipation of energy for a fixed and given load value.

Additionally, the overshoot—corresponding to an overflow of perceived energy—is directly linked to this initial peak. The influence of the trigger initiation system on the overshoot can clearly be visible in Figure 22, with configuration (b) increasing the overshoot value, while configuration (c) decreases it, compared to plain crushing (configuration (a)). Regarding the inner conic crushing (configuration (c)), it can be noted that the overshoot is significantly reduced without drastically reducing the SEA. Furthermore, the dispersion of the SEA for this specific configuration is the lowest, being less than 5% compared to 20–30% for the others, leading to infer a more stable crushing, resulting from a geometric effect of the inner-oriented conic initiation part.

In case of outer crushing, the use of a conic plug initiator (d) to introduce a radial flaring of the tube structure before it is submitted to crushing does not improve the energy absorbing capability, compared to pure and plain crushing (a), as shown in Figures 18

and 22. Configuration (d) does not reduce the overshoot either (Figure 22). Moreover, this configuration worsens the energy absorbing capability as it significantly lowers the SEA value (Figures 18 and 22). At last, the use of the conic plug alone, passing through the tube along its whole length and inducing an axial flaring of the structure (configuration (e)) hardly dissipate any energy, leading to the conclusion that the expansion of the crimping fibers is not a primordial mechanism in composite absorption capability. For this reason, results from configuration (e) will mostly be disregarded in the following discussions.

However, notwithstanding the current results, it is essential to keep in mind that configurations (d) and (e) are highly dependent on the dimensions of the conic plug initiator, which may have been improperly chosen to achieve the goal of reducing the overshoot. A more complete and focused study on more adequate dimensions of the conic slope may be needed, with a series of tests imposing a gradual strain deformation (0.005, 0.010, 0.015, 0.020, 0.025 . . .) for instance.

Tomographic imaging

Post-testing X-ray micro-measurement observations were conducted to observe and determine the damage mechanisms involved during crushing on the inside of the tube wall's thickness. X-ray 3D-micro-computed tomography images were performed using a Micro-Tomography EasyTom 130 machine, manufactured by RX Solutions, France. The tubular specimens were placed at a distance of 91.3 mm from the source. The source has a voxel size of 18 μm . Each specimen was scanned through a 360° rotation using a Varian PaxScan 1313DX imager to capture layer-by-layer 2D X-ray images used for full-scale 3D reconstruction. RX Solutions X-Act 2.0 software was used for 3D reconstruction and post-processing. Due to the samples size and dimensions the maximum possible and workable resolution was 18 μm . The source–object distances (sod) and source–detector distances (sdd) were 91.3 mm and 643.9 mm, respectively, which determine the magnification (sdd/sod) at 7.05. The X-ray voltage and current were set to 60 kV and 133 mA, respectively.

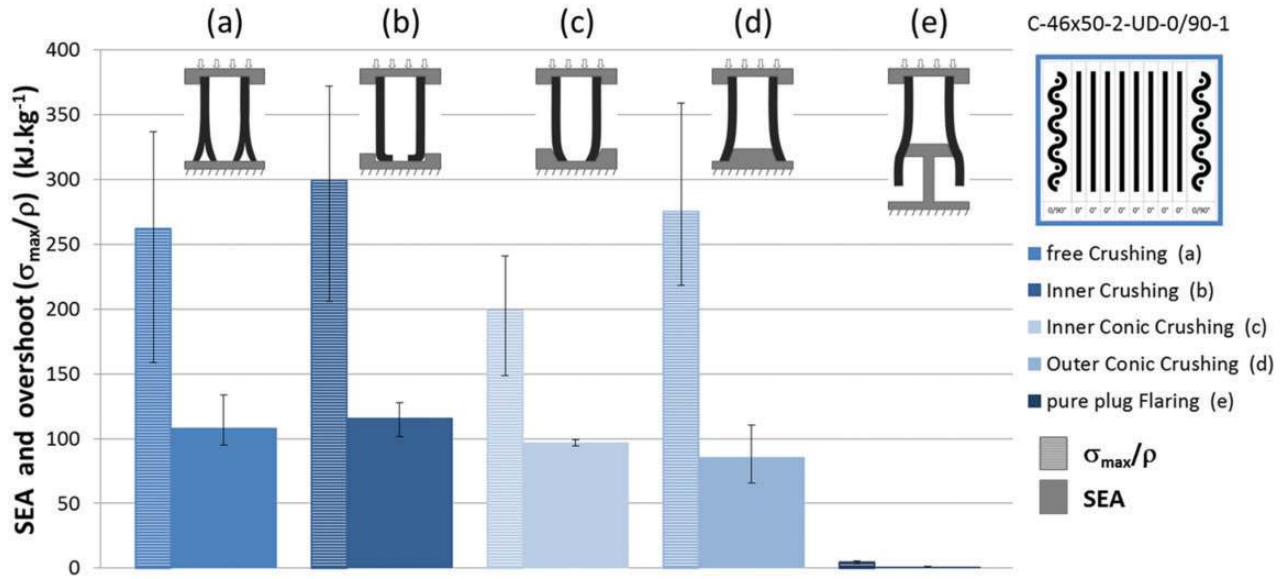


Figure 22. SEA and overshoot values for tube specimen I for the five configurations.

Each sample was scanned for 160 min with 0.6 s per projection.

Figure 23 highlights major occurring damage mechanisms resulting from progressive crushing instigated by quasi-static axial compression load for tube specimen I through the means of tomographic imaging for four different crushing modes ((a), (b), (c), and (d) when referring to Figure 15). Inner (a), (b), (c), and outer (a), (d) splaying of fragmented or un-fragmented parts are clearly visible, as well as debris accumulation.

The high porosity of the tube specimen is also visible, black shaped holes and lines on the inside of the tube's wall, confirming the visual observations from the microscopic images.

The crushing plane surface is schematized by a discontinued line on all pictures in Figure 23. It is strongly suspected that for each tube samples, folded plies at the end of the tube walls between the same part of the tubes and the crushing surface moved back downward when the crushing force was unloaded, due to a spring-back effect. Hence an estimated positioning of the crushing surface appearing to be situated within the tube and entering inside the tube structure. Similarly, positions of the boundary parts and conic-shaped parts were added.

For the first configuration (a), a pyramidal-shaped debris accumulation can be observed at the center under the tube wall, between the tube section and the crushing surface, where the laminate plies spread towards the inside or the outside of the tubular structure. This debris accumulation forms from the void created by the plies splaying from the center under the tube wall then subsequently helps further and heighten this splaying.

At the contact surface between the tube circular section and the plane surface, micro-buckling occurs progressively and successively, resulting in matrix and/or fibers fragmentation for the laminate plies that undergo such splaying. This damage mode increases the debris formation. As observed and mentioned in previous study, the formation and the evacuation or accumulation of debris remains rather random.

For the second test configuration (b), damage mechanisms are similar in type and classification but are all shifted toward the inside of the tube, since the outer wall is encased, leaving no leeway for splayed plies to spread that way. Incidentally, although major occurring damage are the same, their origin varies somewhat. Bending and folding resulting from the compression generate the splaying of the composite plies, and therefore the fracture and fragmentation for those sustaining a higher stress. Fragmentation still generates an important number of debris that varies in forms and shape, but those are freely evacuated from the crushing zone under the tube section to the inside of the tube. They do not form a tip that parts the laminate wall and split it, as observed with the pyramidal debris accumulation on the first configuration.

At the extremity of the tube wall, where the folding appears, outer plies seem to be more submitted to bending, whereas inner plies undergo plain compression and break through intra-laminar fracture.

According to the tomographic imaging, configuration (c) is almost identical to configuration (b) but appears to be less densified at the center, on the inside of the tube's wall. This might explain why no increase of the crushing stress is observed on the crush-displacement curves for that configuration.

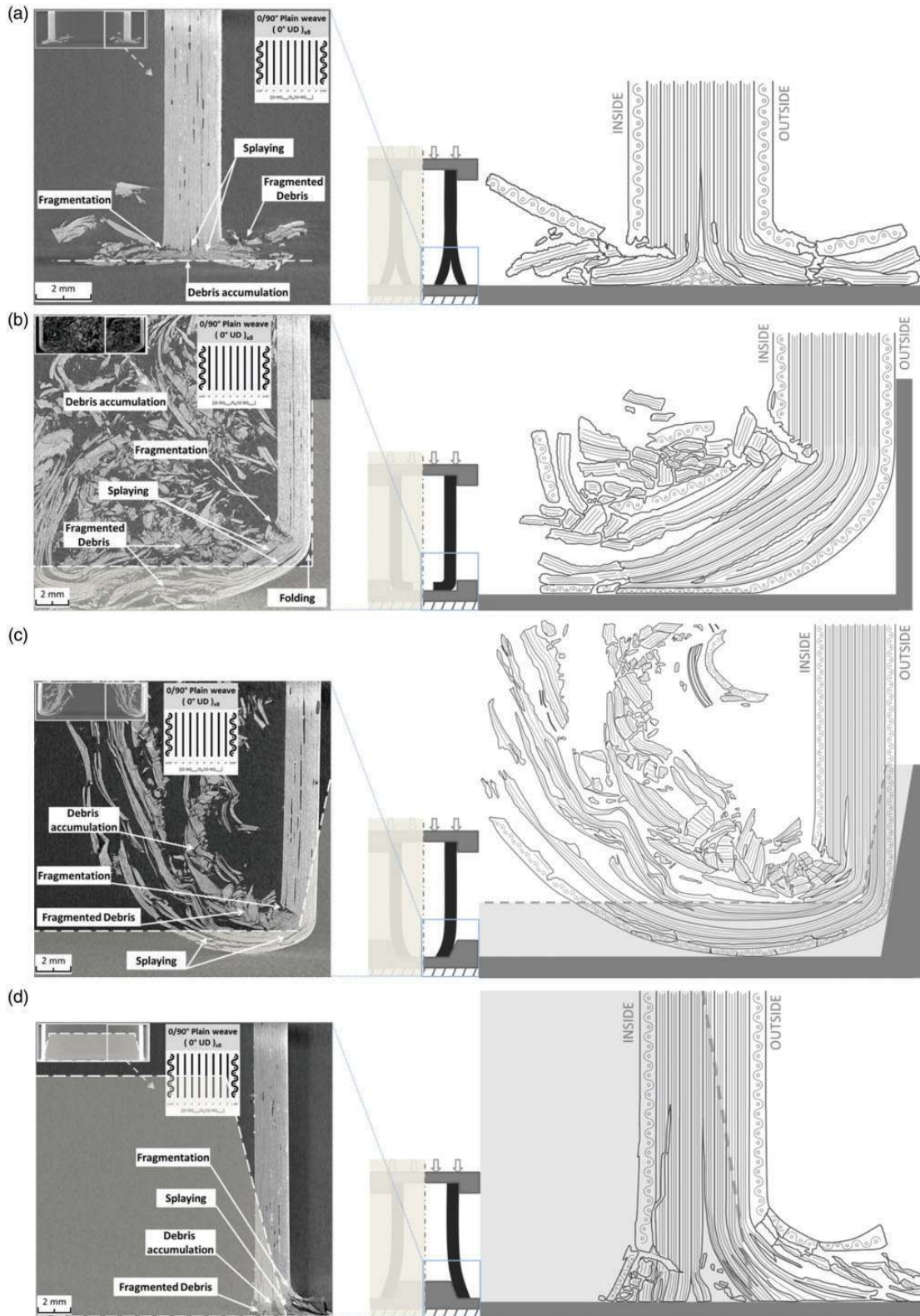


Figure 23. Tomographic images and schematizations of crushed CFRP tubes showing major damage and plies dispersion for specimen I in four configurations ((a), (b), (c) and (d)). (a) Post-testing tomographic image and schematization for tube I in free crushing. (b) Post-testing tomographic image and schematization for tube I in inner crushing. (c) Post-testing tomographic image and schematization for tube I in inner conic crushing. (d) Post-testing tomographic image and schematization for tube I in outer conic crushing.

The inner slope inclination favored the “folding” of the inner fabric ply by guiding it, contrary to configuration (b) where it was more abruptly fractured.

For the last test configuration (d), outer splaying is mainly predominating, since the conic shape blocked the inner splaying and spreading towards the interior of the tube. On the interior side of the tube, splaying is almost nonexistent. However, fragmentation is intensified, with large fractures, of both the fibers and the matrix. Additionally, the tube wall went back to its initial position, once the metallic conic part was withdrawn, due to a vertical spring back effect and the wall’s rigidity.

It appears from images in Figure 23, that for every configuration tested (except configuration (e)), there are always three or four plies damaged by fragmentation while the seven or six remaining plies are only bent in splaying. The 3 or 4 fragmented plies are always inside plies of the tube’s structure.

Those inner plies are the most impacted and the most solicited plies during crushing, creating a localized fragmentation that leads to a localized crushing which characterizes the MCS defined by Israr Ahmad et al.¹⁶ and Rivallant et al.²⁴ This would explain the overall crushing stress ($\sigma_{crushing}$) always averaging around 150 MPa, for every configuration tested (except configuration (e), which underwent no crushing at all.) as displayed in Figure 24. It can be inferred from that observation that this definite number of fragmented plies is optimum in order to optimize the SEA value.

Some notable observations were incidentally made for other tube specimens in other crushing configurations, as pointed out in the following section.

For the inner-crushing configuration (b), tube specimens 3, 4, and 5 displayed two major modes of failure. Figure 25 presents that distinction in failure behavior mode observed for some samples in inner-crushing configuration (b) using tube specimen 3 as an example. Those two modes, namely catastrophic failure and progressive crushing, were reported to occur by Thornton and Thornton^{2,18} and previously illustrated in general crushing case by Figure 1 (a) and (b).

Although in most instances, tube specimens 3, 4, and 5 behaved according to a usual progressive crushing mode, in some cases, they underwent catastrophic failure from a middle point of the tubular structure and without undergoing progressive crushing from one end. Visual illustrations of the catastrophic failure mode demonstrated by those samples are given with pictures in Figure 26.

This unwanted failure mode drastically lowers the SEA value for these samples in this particular configuration to 13.1 kJ.kg^{-1} for specimen 3 and 26.5 and 27.4 kJ.kg^{-1} for specimen 4 and 5, while they stand at 52.8 , 44.7 , and 52.8 kJ.kg^{-1} , respectively, when progressive crushing occurs in this configuration.

The ratio of catastrophic failure stands at 25%, 33%, and 50% for tube specimens 3, 4, and 5, respectively, in inner-crushing configuration (b), when these tubes displayed a 99.8% progressive crushing successful behavior in all other configurations.

In practical terms, inner-crushing configurations reduced the production and scattering of debris, as the undamaged part of the tube act as a sheath as can be seen in pictures in Figure 17. To that extend, tube specimens 4 and 5 (the two specimens that have an

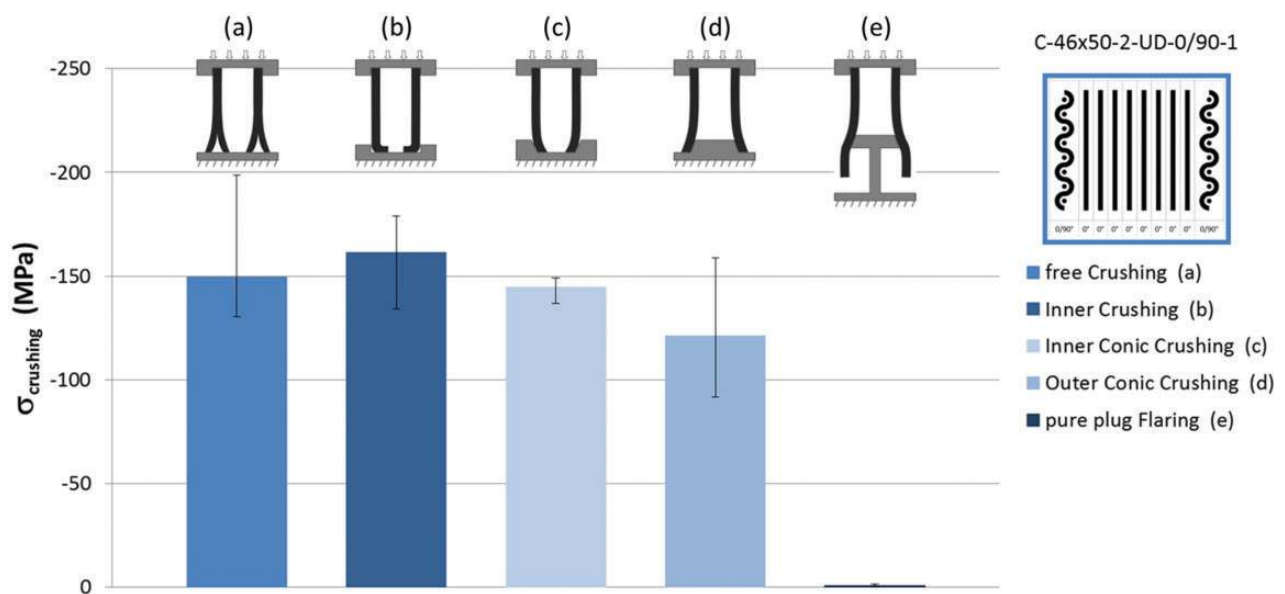


Figure 24. MCS values for tube specimen I for the five configurations.

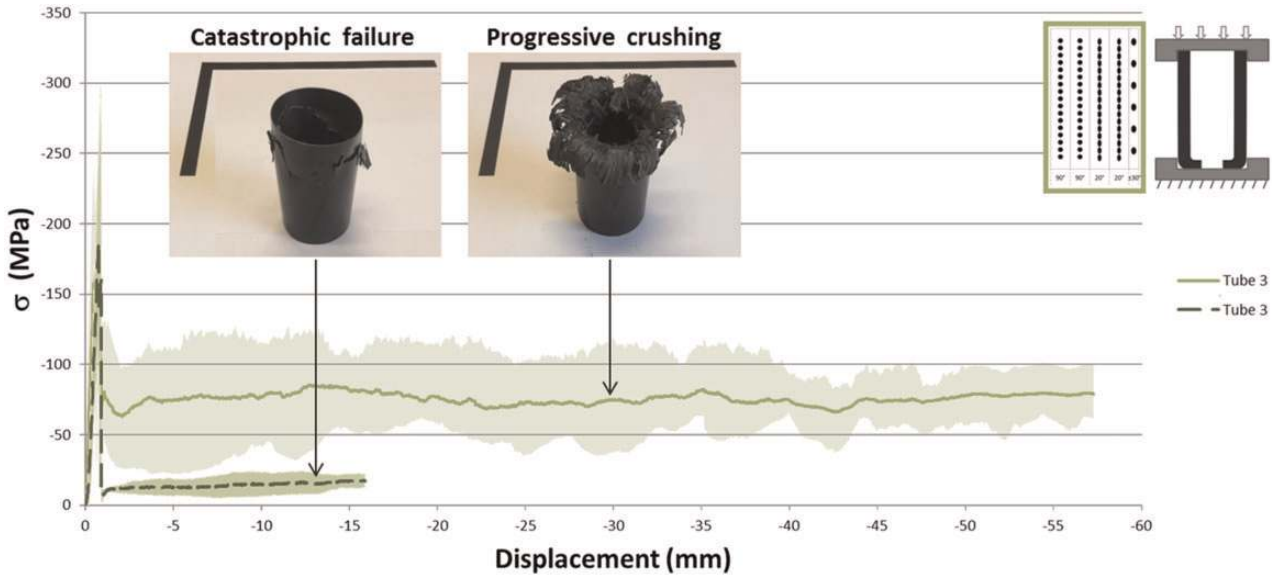


Figure 25. Stress–displacement curve and dispersion for tube specimen 3 and inner-crushing configuration.



Figure 26. Pictures of CFRP tube specimens 3, 4, and 5 which underwent catastrophic failure for inner-crushing configuration (b).

aramid cover on top of the carbon structure) do not present any interest regarding the SEA value, but the aramid cover acts as a girdle, helping in folding and containing the fragmented parts, both in case of inner

and outer crushing. This comes at the expense of a lower compression stiffness and a lower tubular section to conserve a similar density, when comparing with tube sample 3 and referring to Table 1.

Figure 27 summarizes the SEA average values obtained for all tube samples (1 to 5) in all configurations ((a) to (e)), with dispersion marks for each testing.

For tube specimen 1 inner-crushing (b) seems to enhance the SEA while inner-conic crushing (c) lowers the value (for the chosen conic dimensions). A complementary study on the conic slope inclination might be needed to test different angle dimensions and confirm that result.

For the tube specimen 2, inner-crushing (b) enhances the SEA and inner-conic crushing (c) seems to improve it a little more (with the margin of dispersion taken into account). This improvement might come from the 90°-oriented plies that are more solicited in confined compression. As a result, the overall crushing stress increases and therefore so does the SEA.

Tube specimen 3 performs the most irregularly. In addition to the catastrophic failure mode observed for configuration (b)—which has been discarded for the SEA average calculation in Figure 27—tube specimen 3 shows the biggest dispersion, especially in configuration (b, inner crushing). The lowest SEA values obtained for this sample may be the result of some crushing instabilities, which might be the consequence of the small thickness of the tube’s wall, as that specimen displays the thinnest wall thickness when referring to Table 1. Too thin wall thickness may lead to some unstable crushing phenomena and most notably affect the buckling modes.

Inner-conic crushing (c) seems to work better for specimens with 90°-oriented fibers (specimens 2, 4, and 5, except specimen 3) for the same reasons mentioned above (i.e. confined compression and adequate tube wall thickness), while it can also be noted that they all contain some plies with a fiber orientation at 0° or close to 0° (specimen 2 has 0°-oriented fibers; specimens 4 and 5 have 20°-oriented fibers).

It can also be surprisingly noted that tube specimens 4 and 5 performed well in configuration (c) whereas tube 3 performed poorly in that configuration and that they performed poorly on any other configurations too. This is all the more surprising as they are both covered with aramid layer(s) and that aramid fibers are known to withstand weakly in compression. This can be explained by their relatively bigger thickness (Table 1 and Figure 5), about twice as much as tube 3, and the increase of 20°-oriented plies in number, doubling from specimen 3 (Figure 5).

For all samples (1 to 5), outer-conic crushing (d) lowers the SEA value and degrades the structure absorbing capacity. Failure phenomena involved are primarily the same as described by Hull¹⁹ and presented in Figure 3. For this configuration, while fiber rupture in traction is energetically very dissipative, it is also very localized, whereas crushing, which is slightly less dissipative, could repeatedly happen on a whole area.

The difference in results between inner and outer crushing (both in plain and conical configurations) is fully in accordance with the statement formulated by

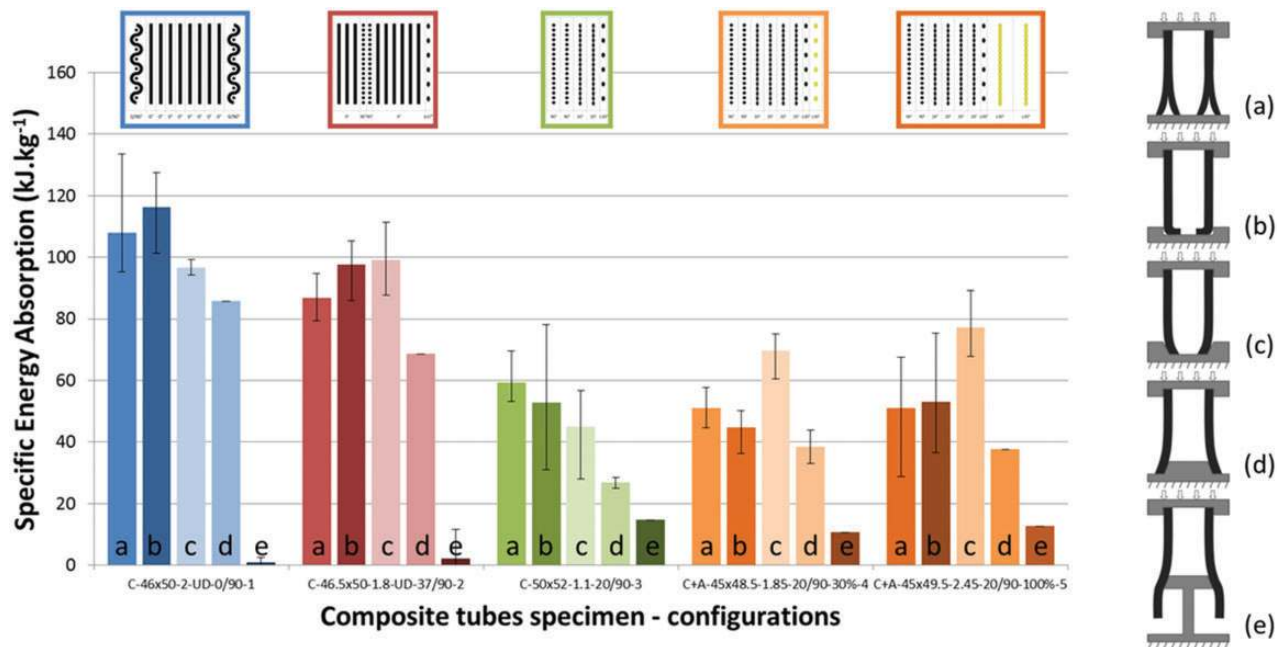


Figure 27. SEA average values for the five CFRP tube specimens submitted to axial crushing in five configurations.

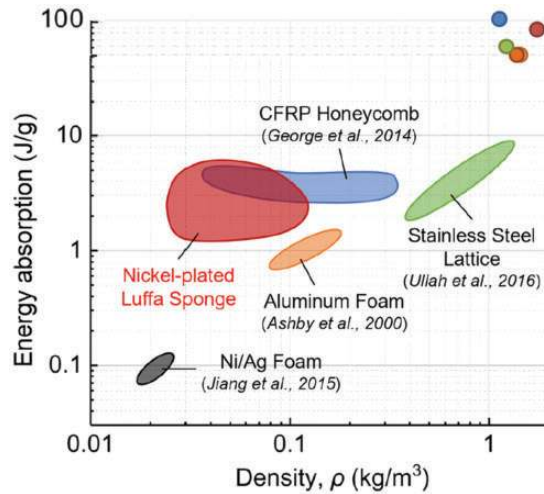


Figure 28. Ashby chart of the energy absorption over density for the five CFRP tubes tested compared with other materials (adapted from Eshkoor et al.⁵⁵).

Brighton et al.²¹ on the relation between cracks density and the radius of curvature of the splayed parts.

Figure 28 displays an Ashby chart of the energy absorption over density with the position of the five CFRP tubes, compared with other materials. The energy absorption value of the five tubes corresponds to the energy resulting from the free crushing configuration (configuration (a)). It can be noted that although the density of the materials is higher for the tube specimens compared with other materials, the energy absorbed is much greater.

Conclusions

Quasi-static axial crushing tests were performed on composite circular tubes with five different structural compositions and using five different trigger initiation configurations.

SEA values up to 140 kJ.kg^{-1} were obtained, achieving better than most instances from the literature, averaging around 50 kJ.kg^{-1} and reaching up to around 100 kJ.kg^{-1} for braided carbon/epoxy structures.

Specimens with 0° -oriented fibers in the axial loading direction achieved better in energy absorption than specimens with no fibers in that direction. It has consequently been established that in static loading, a unidirectional laminate oriented at 0° and stabilized by woven plies strongly meets the expectations in terms of energy dissipation. Incidentally, an inner constrained containment is more effective in most cases, reducing the initial peak load without drastically reducing the SEA value.

Woven reinforcement on the inner and outer wall structure proved more effective than solid strengthening supports such as metal constraints or poured resin in

providing stability to the structure. Additionally, the woven plies help containing the 0° -oriented fibers from splaying and flaring too easily. Moreover, as such woven plies are structurally required for stability reasons, it is opportune to try and put them in beneficial use, hence the inner oriented crushing concepts, which load and stress these fibers in crushing.

However, the additional aramid draping was proven needless in term of energy absorbing capacity. Yet this overlapping covering may be valuable in acting as a net to refrain outer spreading by directing splayed chunks and debris towards the inside and keep brittle parts within the inside of the tubular structure, avoiding expelled debris, as could be required in an aeronautical context.

Potential applications may include energy absorption systems for airplane passenger seats, or helicopter seats, as well as applications in railway transportation vehicles (trains, wagons, cars...).

In order to complete this study and provide complementary understanding regarding the crushing of fiber-reinforced composite tubes and SEA enhancement, considerations may be given to the following actions:

- varying the strain rate and conducting a study on dynamic crushing;
- varying the slope inclination and the conic dimensions, especially for the inner-conic concept;
- chamfering the samples and combining that trigger initiation technique with the presented boundary conditions;
- using mechanically known fibers and materials, that is to say constituents for which properties are independently tested and identified to permit the best selection.

Acknowledgements

Special thanks are addressed to the CRITT Mécanique & Composites of Toulouse for assisting in performing the tomographic imaging used in this article.

Declaration of Conflicting Interests

The author(s) declared no potential conflicts of interest with respect to the research, authorship, and/or publication of this article.

Funding

The author(s) disclosed receipt of the following financial support for the research, authorship, and/or publication of this article: Financial support for this study was acquired thanks to FEDER funds through the joint project SKYSEAT co-funded by ARTEC Aerospace Company, the Occitanie—Pyrénées-Méditerranée Region (ex-Midi-Pyrénées Region) and the ISAE-SUPAERO.

ORCID iD

C Bouvet  <https://orcid.org/0000-0003-2637-9170>

References

1. Farley GL. Energy absorption of composite materials. *J Compos Mater* 1983; 17: 267–279.
2. Thornton PH. The crush of fiber-reinforced plastics. In: Cheremisinoff NP (ed.) *Handbook of ceramics and composites volume 1: synthesis and properties*. New York, New York: Marcel Dekker Inc., 1990, pp.307–337.
3. Hamada H, Ramakrishna S and Satoh H. Crushing mechanism of carbon fibre/PEEK composite tubes. *Composites* 1995; 26: 749–755.
4. Mamalis AG, Robinson M, Manolakos DE, et al. Crashworthy capability of composite material structures. *Compos Struct* 1997; 37: 109–134.
5. Thornton PH, Harwood JJ and Beardmore P. Fiber-reinforced plastic composites for energy absorption purposes. *Compos Sci Technol* 1985; 24: 275–298 **[AQ4]**.
6. Jacob GC, Fellers JF, Simunovic S, et al. Energy absorption in polymer composites for automotive crashworthiness. *J Compos Mater* 2002; 36: 813–850.
7. Bisagni C, Di Pietro G, Frascini L, et al. Progressive crushing of fiber-reinforced composite structural components of a Formula One racing car. *Compos Struct* 2005; 68: 491–503.
8. Kim JS, Yoon HJ, Lee HS, et al. Energy absorption characterization of composite tubes for railway application. In: *Proceedings of the 17th international conference on composite materials (ICCM)*, Edinburgh, Scotland, UK, 27–31 July 2009 **[AQ5]**.
9. Kim J-S, Yoon H-J and Shin K-B. A study on crushing behaviors of composite circular tubes with different reinforcing fibers. *Int J Impact Eng* 2011; 38: 198–207.
10. Farley GL and Jones RK. Energy-absorption capability of composite tubes and beams. NASA Technical Memorandum, NASA TM-101634 – AVSCOM Technical Report 89B.003, AVSCOM TR-89-B-003, NASA Langley Research Center, Hampton, VA, USA – Aerostructures Directorate USAARTA (AVSCOM), Hampton, VA, USA, September 1989.
11. Heimbs S, Strobl F, Middendorf P, et al. Composite crash absorber for aircraft fuselage applications. *WIT Transac Built Environ* 2010; 113: 3–14.
12. Farley GL. Relationship between mechanical property and energy-absorption trends for composite tubes. NASA Technical Paper, NASA-TP-3284, 19930007348, Langley Research Center, Hampton, VA, USA, December 1992.
13. McCarthy MA and Wiggenraad JFM. Numerical investigation of a crash test of a composite helicopter subfloor structure. *Compos Struct* 2001; 51: 345–359.
14. Wang Y, Feng J, Wu J, et al. Effects of fiber orientation and wall thickness on energy absorption characteristics of carbon-reinforced composite tubes under different loading conditions. *Compos Struct* 2016; 153: 356–368.
15. Cauchi Savona S and Hogg PJ. Effect of fracture toughness properties on the crushing of flat composite plates. *Compos Sci Technol* 2006; 66: 2317–2328.
16. Israr Ahmad HAB, Rivallant S and Barrau J-J. Experimental investigation on mean crushing stress characterization of carbon–epoxy plies under compressive crushing mode. *Compos Struct* 2013; 96: 357–364.
17. Israr Ahmad Hab, Rivallant S, Bouvet C and Barrau J-J. Finite element simulation of 0°/90° CFRP laminated plates subjected to crushing using a free-face-crushing concept. *Compos Part A: Appl Sci Manuf* 2014; 62: 16–25.
18. Thornton PH. Energy absorption in composite structures. *J Compos Mater* 1979; 13: 247–262.
19. Hull D. A unified approach to progressive crushing of fibre-reinforced composite tubes. *Compos Sci Technol* 1991; 40: 377–421.
20. Farley GL and Jones RM. Crushing characteristics of continuous fiber-reinforced composite tubes. *J Compos Mater* 1992; 26: 37–50.
21. Brighton A, Forrest M, Starbuck M, et al. Strain rate effects on the energy absorption of rapidly manufactured composite tubes. *J Compos Mater* 2009; 43: 2183–2200.
22. Pinho ST, Camanho PP and De Moura MF. Numerical simulation of the crushing process of composite materials. *Int J Crashworthiness* 2004; 9: 263–276.
23. Supian ABM, Sapuan SM, Zuhri MYM, et al. Hybrid reinforced thermoset polymer composite in energy absorption tube application: a review. *Def Technol* 2018; 14: 291–305.
24. Rivallant S, Bouvet C and Hongkarnjanakul N. Failure analysis of CFRP laminates subjected to compression after impact: FE simulation using discrete interface elements. *Compos Part A: Appl Sci Manuf* 2013; 55: 83–93.
25. Fan Z, Lu G and Liu K. Quasi-static axial compression of thin-walled tubes with different cross-sectional shapes. *Eng Struct* 2013; 55: 80–89.
26. Esnaola A, Ulacia I, Aretxabaleta L, et al. Quasi-static crush energy absorption capability of E-glass/polyester and hybrid E-glass–basalt/polyester composite structures. *Mater Design* 2015; 76: 18–25.
27. Gliszczynski A and Kubiak T. Progressive failure analysis of thin-walled composite columns subjected to uniaxial compression. *Compos Struct* 2017; 169: 52–61.
28. Palanivelu S, Van Paepegem W, Degrieck J, et al. Comparative study of the quasi-static energy absorption of small-scale composite tubes with different geometrical shapes for use in sacrificial cladding structures. *Polym Test* 2010; 29: 381–396.
29. Palanivelu S, Van Paepegem W, Degrieck J, et al. Crushing and energy absorption performance of different geometrical shapes of small-scale glass/polyester composite tubes under quasi-static loading conditions. *Compos Struct* 2011; 93: 992–1007.
30. Kathiresan M, Manisekar K and Manikandan V. Crashworthiness analysis of glass fibre/epoxy laminated thin walled composite conical frusta under axial compression. *Compos Struct* 2014; 108: 584–599.
31. Lau STW, Said MR and Yaakob MY. On the effect of geometrical designs and failure modes in composite axial crushing: a literature review. *Compos Struct* 2012; 94: 803–812.

32. David M, Johnson AF and Voggenreiter H. Analysis of crushing response of composite crashworthy structures. *Appl Compos Mater* 2013; 20: 773–787.
33. Elgalai AM, Mahdi E, Hamouda AMS, et al. Crushing response of composite corrugated tubes to quasi-static axial loading. *Compos Struct* 2004; 66: 665–671.
34. Farley GL. Effect of fiber and matrix maximum strain on the energy absorption of composite materials. *J Compos Mater* 1986; 20: 322–334.
35. Hamada H, Coppola JC, Hull D, et al. Comparison of energy absorption of carbon/epoxy and carbon/PEEK composite tubes. *Composites* 1992; 23: 245–252.
36. Ramakrishna S and Hull D. Energy absorption capability of epoxy composite tubes with knitted carbon fibre fabric reinforcement. *Compos Sci Technol* 1993; 49: 349–356.
37. Hamada H and Ramakrishna S. Scaling effects in the energy absorption of carbon-fiber/PEEK composite tubes. *Compos Sci Technol* 1995; 55: 211–221.
38. Chiu CH, Tsai KH and Huang WJ. Effects of braiding parameters on energy absorption capability of triaxially braided composite tubes. *J Compos Mater* 1998; 32: 1964–1983.
39. Beard SJ and Chang F-K. Energy absorption of braided composite tubes. *Int J Crashworthiness* 2002; 7: 191–206.
40. Song H-W, Du X-W and Zhao G-F. Energy Absorption Behavior of Double-Chamfer Triggered Glass/Epoxy Circular Tubes. *J Compos Mater* 2002; 36: 2183–2198.
41. Huang J-C and Wang X-W. Effect of the SMA trigger on the energy absorption characteristics of CFRP circular tubes. *J Compos Mater* 2009; 44: 639–651.
42. Palanivelu S, Van Paepegem W, Degrieck J, et al. Experimental study on the axial crushing behaviour of pultruded composite tubes. *Polym Test* 2010; 29: 224–234.
43. Priem C, Othman R, Rozycki P, et al. Experimental investigation of the crash energy absorption of 2.5D-braided thermoplastic composite tubes. *Compos Struct* 2014; 116: 814–826.
44. Priem C, Rozycki P, Othman R, et al. Crash of 3D-braided thermoplastic tubes: numerical and analytical tools for behaviour prediction. In: *Proceedings of the XIII international conference on computational plasticity. Fundamentals and applications – COMPLAS XIII*, Barcelona, Spain, 1–3 September 2015.
45. McGregor CJ, Vaziri R, Poursartip A, et al. Axial crushing of triaxially braided composite tubes at quasi-static and dynamic rates. *Compos Struct* 2016; 157: 197–206.
46. Tong Y and Xu Y. Improvement of crash energy absorption of 2D braided composite tubes through an innovative chamfer external triggers. *Int J Impact Eng* 2018; 111: 11–20.
47. Yang Y, Ahmed K, Zhang R, et al. A study on the energy absorption capacity of braided rod composites. *Compos Struct* 2018; 206: 933–940.
48. Mou HL, Xie J, Su X, et al. Crashworthiness experiment and simulation analysis of composite thin-walled circular tubes under axial crushing. *Mech Compos Mater* 2019; 55: 121–134.
49. Jiménez MA, Miravete A, Larrode E, et al. Effect of trigger geometry on energy absorption in composite profiles. *Compos Struct* 2000; 48: 107–111.
50. Mamalis AG, Manolakos DE, Ioannidis MB, et al. On the response of thin-walled CFRP composite tubular components subjected to static and dynamic axial compressive loading: experimental. *Compos Struct* 2005; 69: 407–420.
51. Xiao X, Botkin ME and Johnson NL. Axial crush simulation of braided carbon tubes using MAT58 in LS-DYNA. *Thin-Walled Struct* 2009; 47: 740–749.
52. Xiao X, McGregor CJ, Vaziri R, et al. Progress in braided composite tube crush simulation. *Int J Impact Eng* 2009; 36: 711–719.
53. McGregor CJ, Vaziri R and Xiao X. Finite element modelling of the progressive crushing of braided composite tubes under axial impact. *Int J Impact Eng* 2010; 37: 662–672.
54. Bambach MR. Axial capacity and crushing of thin-walled metal, fibre-epoxy and composite metal-fibre tubes. *Thin-Walled Struct* 2010; 48: 440–452.
55. Eshkoor RA, Oshkovr SA, Sulong AB, et al. Comparative research on the crashworthiness characteristics of woven natural silk/epoxy composite tubes. *Mater Design* 2013; 47: 248–257.
56. Taşan A, Acar E, Güler MA, et al. Optimum crashworthiness design of tapered thin-walled tubes with lateral circular cutouts. *Thin-Walled Struct* 2016; 107: 543–553.
57. De Carvalho NV, Pinho ST and Robinson P. An experimental study of failure initiation and propagation in 2D woven composites under compression. *Compos Sci Technol* 2011; 71: 1316–1325.
58. Hamada H, Ramakrishna S and Sato H. Effect of fiber orientation on the energy absorption capability of carbon fiber/PEEK composite tubes. *J Compos Mater* 1996; 30: 947–963.
59. Carruthers JJ, Kettle AP and Robinson AM. Energy absorption capability and crashworthiness of composite material structures: a review. *Appl Mech Rev* 1998; 51: 635–649.
60. Yin S, Wang H, Li J, et al. Light but tough bio-inherited materials: luffa sponge based nickel-plated composites. *J Mech Behav Biomed Mater* 2019; 94: 10–18 **IAQ6**.